DISCLAIMER

This report was prepared as an account of work sponsored by an agency of the United States Government. Neither the United States Government nor any agency thereof, nor any of their employees, makes any warranty, express or implied, or assumes any legal liability or responsibility for the accuracy, completeness, or usefulness of any information, apparatus, product, or process disclosed, or represents that its use would not infringe privately owned rights. Reference herein to any specific commercial product, process, or service by trade name, trademark, manufacturer, or otherwise does not necessarily constitute or imply its endorsement, recommendation, or favoring by the United States Government or any agency thereof. The views and opinions of authors expressed herein do not necessarily state or reflect those of the United States Government or any agency thereof. Reference herein to any social initiative (including but not limited to Diversity, Equity, and Inclusion (DEI); Community Benefits Plans (CBP); Justice 40; etc.) is made by the Author independent of any current requirement by the United States Government and does not constitute or imply endorsement, recommendation, or support by the United States Government or any agency thereof.

Argonne NATIONAL LABORATORY

Advanced Reactor Safeguards & Security

Assessment of Flow-Enhanced Electrochemical Sensor Testing and Deployments

Prepared for
US Department of Energy

William Doniger, Matthew Jubinsky, Colin Moore, Nora Shaheen, Nathaniel Hoyt

Argonne National Laboratory

September 30, 2024
ANL/CFCT-24/29

About Argonne National Laboratory

Argonne is a U.S. Department of Energy laboratory managed by UChicago Argonne, LLC under contract DE-AC02-06CH11357. The Laboratory's main facility is outside Chicago, at 9700 South Cass Avenue, Argonne, Illinois 60439. For information about Argonne and its pioneering science and technology programs, see www.anl.gov.

[This page intentionally left blank]

ABSTRACT

The goal of our activities in FY24 was to enable advanced materials accountancy for molten salt reactors (MSRs) through the development and optimization of robust flow-enhanced electrochemical sensors (FEES) using a safeguards-focused sensor testing platform called the modular flow instrumentation testbed (MFIT). Flow-enhanced electrochemical sensors are a type of electroanalytical sensor that have been developed at Argonne National Laboratory to be installed directly into MSR flow conduits to make measurements of the salt composition. These sensors represent a significant improvement in capabilities compared to earlier electroanalytical sensors that instead can only be operated in quiescent conditions. Previous work has focused on testing of the FEES in flowing conditions provided by the MFIT to assess the accuracy and precision of the sensor measurements. This year, the FEES technical readiness was increased by (1) demonstrating the use of optimized sensor techniques to achieve measurements in very high-concentration MSR-relevant salts, (2) leveraging new multimodal sensors and automation approaches to reduce measurement uncertainties, and (3) fabricating and deploying sensors to industrial partners to improve their ability to make measurements in challenging environments. Additionally, we also ran the sensors during complex system operations involving combined flow and purification activities to demonstrate safeguards-relevant measurements during online processing for MSRs.

CONTENTS

ABSTRACT iii
CONTENTS iv
FIGURES v
ACRONYMS AND ABBREVIATIONS vii
ACKNOWLEDGEMENTS viii

1. INTRODUCTION 1

2. ELECTROCHEMICAL RESPONSE TO HYDRODYNAMIC CONDITIONS 2

3. EXPERIMENTAL METHODS AND SETUP 4
3.1 MFIT System overview 4
3.2 Miniature-MFIT System Overview 5
3.3 Monitoring Capabilities within the Modular Flow Instrumentation Testbed 7
3.3.1 Flow enhanced electrochemical sensors 7
3.3.2 Multielectrode array voltammetry sensors 8
3.3.3 Multielectrode array level sensors 8
3.3.4 Miscellaneous sensors 9

4. Assessment of FEES in high concentration actinide salts 12
4.1.1 UCl_3 Measurements in High-Concentration LiCl-KCl-UCl_3 12
4.1.2 High-Concentration UCl_3 Salt Production 19

5. FEES Sensor Performance Improvements and Multimodal Monitoring 22
5.1 Multimodal Sensor Development in the Miniature-Modular Flow Instrumentation Testbed 22
5.2 Multimodal Sensor Development in the Modular Flow Instrumentation Testbed 26

6. Multimodal Monitoring Demonstration During Complex Flow System Operations 30

7. FEES Sensor Deployments 34
7.1 Flow Enhanced Electrochemical Sensors at Kairos Power, LLC FLiBe salt test loop 34
7.2 Sensor Deployment to TerraPower LLC 36

8. CONCLUSIONS 38
REFERENCES 39

FIGURES

Figure 1. Schematic and rendering of sensor design in center section of MFIT transfer line [9]. 2

Figure 2. Theoretical current response for soluble-soluble reaction induced by applied positive potential [9]....3

Figure 3. Pictures of (a) MFIT complete with heater assemblies, sensors and insulation installed into an (b) inert atmosphere glovebox [9]....5

Figure 4. Mini-MFIT (a) rendering and (b) assembly without the furnace lid and (c) schematic of sensors and fluid flow path [9]. 6

Figure 5. Gas control system (left) and Mini-MFIT system (right) installed in a non-radiological glovebox [9]....6

Figure 6. Flow enhanced electrochemical sensor current response at a mass flow rate controller setpoint of 3 slpm. 7

Figure 7. Mini-MFIT salt level sensor (a) continuity measurement device, (b) electrode array sensor, and (c) diagram of salt level sensor placement in the MINI-MFIT salt tank [9]. 9

Figure 8. Multielectrode array level sensor (MALS) digital interface software [9]. 9

Figure 9. Modular flow instrumentation testbed mass flow controller, pressure transducer, and thermocouple measurements during multiple salt transfers at various mass flow controller setpoints. 10

Figure 10. Comparison of ultrasonic level sensor and multielectrode array level sensor during incremental changes in water height of 7 mm at room temperature. 11

Figure 11. LiCl-KCl-UCl_3 (left) 72.3 wt% UCl_3 and (right) 60.8 wt% UCl_3 before and after electroanalytical experiments. 12

Figure 12. Cyclic voltammogram of LiCl-KCl and LiCl-KCl-UCl_3(60.8 wt%) at 600 ˚C. 14

Figure 13. Cyclic voltammetry of LiCl-KCl-UCl_3(66.6 wt %) at 600 ˚C (a) at various potential scan rates, (b) the peak current vs. the square root of scan rate, and (c) the anodic peak potential at various scan rates. 15

Figure 14. Simulated cyclic voltammograms showing the effects increasing solution resistance [16]. 15

Figure 15. Ten repeated cyclic voltammograms of LiCl-KCl-UCl_3 (46 wt% U) at 600 ˚C. The potential scan rate is 3000 mV/sec and there is 5-minute delay between voltammograms. 16

Figure 16. Linear sweep voltammetry of LiCl-KCl-UCl_3(66.6 wt %) at 600 ˚C using a multielectrode array voltammetry sensor (MAVS) to (a) obtain the current response from each electrode (in triplicate), (b) determination of electrode surface area from the anodic peak current, and (c) all cyclic voltammograms after surface area correction. Potential scan rate is 3000 mV s^{-1}. The counter electrode is a 2 mm tungsten rod. The reference electrode is a 1 mm diameter tungsten quasi-reference electrode (QRE). 17

Figure 17. Peak Current density vs. UCl_3 concentration in LiCl-KCl-UCl_3 determined with a multielectrode array sensor at 600 ˚C. 18

Figure 18. Images of a) the NaCl-$ZnCl_2$ and b) the resulting NaCl-UCl_3 from the uranium chlorination experiment. The depleted uranium ingot c) before and d) after reaction with $ZnCl_2$ and the copper mesh e) before and f) after reacting with Zn vapor.....20

Figure 19. Depleted uranium powered mesh obtained from storage within an inert atmosphere container. 21

Figure 20. Cyclic voltammogram of stationary NaCl-KCl-$MgCl_2$ with corrosion products at 500 °C using a multielectrode array voltammetry sensor (MAVS). 23

Figure 21. Miniature-MFIT gas control system Ar gas mass flow rate and vacuum pressure during salt flow tests at various mass flow rate flow rate setpoints. 24

Figure 22. Miniature-MFIT multi-electrode array level sensor (MALS) flow rate measurements of NaCl-KCl-MgCl2 at 500 ˚C. 24

Figure 23. Current response to an oxidizing voltage in flowing NaCl-KCl-$MgCl_2$ with corrosion products at 500 °C. 25

Figure 24. FEES average current response to constant applied potential during Miniature-MFIT salt flow at various flow rates. 25

Figure 25. Flow enhanced electrochemical sensor current response as a function of a) mass flow controller setpoints and b) FEES sensor flow rate measurements at each mass flow controller setpoint in standard liters per minute. 26

Figure 26. Multielectrode array level sensor (MALS) measured flow rate vs. the mass flow controller setpoint.....27

Figure 27. Flow enhanced electrochemical sensor current response various flow rates. The uncorrected data is plotted against flow rates measured using the FEES sensor. The corrected data is plotted against flow rate measurements using the multielectrode array level sensor (MALS). 27

Figure 28. Flow enhanced electrochemical sensor current response at different U^{3+} concentrations and flow rates. Lines represent the nonlinear-surface fit for the sensor response function. 28

Figure 29. Parity plot of uranium concentration from process knowledge and uranium concentration measured across a full range of flow rates using the FEES. 29

Figure 31. Depleted uranium-zirconium-molybdenum fuel rod used for salt processing studies in the MFIT.....30

Figure 31. Cyclic voltammetry of NaCl-KCl-$MgCl_2$-UCl_3 (3 wt. % UCl_3) at 500 ˚C after various exposure times to a depleted uranium fuel rod. Scan rate 1000 mV/sec. 31

Figure 32. Multielectrode array voltammetry sensor (MAVS) measurements of NaCl-KCl-$MgCl_2$-UCl_3 (3 wt. % UCl_3) during depleted uranium metal contacting including (a) the height of the salt reltive to the MAVS sensor, (b) the average salt redox potential, (c) the reduction peak potential of U/U(III), Cr/Cr(II), and Fe/Fe(II), (d) the cathodic peak current density of of U/U(III), Cr/Cr(II), and Fe/Fe(II) reactions, and (e) the concentration of U(III), Cr(II), and Fe(II). 33

Figure 33. Kairos Power's FLiBe salt test loop 34

Figure 34. Argonne National Laboratory's custom 12-channel multiplexer for controlling electrochemical sensors in the Kairos test loop. 34

Figure 35. In-line flow enhanced electrochemical sensors installed in Kairos Power's test loop. 35

Figure 36. Temperatures near the two in-line electrochemical sensors. 35

Figure 37. In-line electrochemical sensor voltammetry measurements of circulating FLiBe salt in the Kairos test loop. 36

Figure 38. A pair of multielectrode array voltammetry sensors (MAVS) for deployment at TerraPower, LLC. Argonne National Laboratory's custom 4-channel Multiplexer for controlling two multielectrode array voltammetry sensors (MAVS). 37

ACRONYMS AND ABBREVIATIONS

ANL	Argonne National Laboratory
CA	Chronoamperometry
CV	Cyclic Voltammogram
DOE	US Department of Energy
FEES	Flow-enhanced Electrochemical Sensor
MAVS	Multielectrode Array Voltammetry Sensor
MALS	Multielectrode Array Level Sensors
MC&A	Materials Control and Accounting
MFC	Mass Flow Controller
MFR	Measured Flow Rate
MFIT	Modular Flow Instrumentation Testbed
MSR	Molten Salt Reactor
PT	Pressure Transducer
slpm	Standard Liters Per Minute
TC	Thermocouple

ACKNOWLEDGEMENTS

This report serves as the deliverable for Milestones M3RS-24AN0401071 and M4RS-24AN0401073 that are a part of Work Package RS-24AN040106 (*Flow-Enhanced Sensors for MSRs – ANL*).

This report was produced under the auspices of the US DOE Office of Nuclear Energy's Advanced Reactor Safeguards and Security Program, Dr. B. Cipiti, National Technical Director and D. Warner, Program Manager.

This work was conducted at Argonne National Laboratory and supported by the U.S. Department of Energy, Office of Nuclear Energy, under Contract DE-AC02-06CH11357.

Advanced Reactor Safeguards and Security Program

ASSESSMENT OF FLOW-ENHANCED ELECTROCHEMICAL SENSOR TESTING AND DEPLOYMENTS

1. INTRODUCTION

In support of the DOE Department of Nuclear Engineering's Advanced Reactor Safeguards & Security program, Argonne National Laboratory has developed novel sensors and a versatile testbed to support the development of material control and accountancy (MC&A) technologies for liquid-fueled molten salt reactors (MSRs). Many monitoring approaches have been proposed for MC&A for MSRs including electrochemical sensors, [1], [2], [3] in-line spectroscopic sensors [4], [5] gamma and neutron measurements [6], alpha spectroscopy [7] and destructive analysis techniques [8]. In-line and on-line tools are particularly advantageous due to their near real-time measurements, but MSRs create challenging conditions that make it difficult to design and operate safeguards-relevant tools that can be operated for long periods without failure of the sensing mechanism.

The high flow velocities encountered in an MSR reactor's primary and secondary fluid streams are a significant challenge for operations of sensors that monitor the salt composition. For example, the flux of fluid across an electrode that is part of a traditional electroanalytical sensor can cause large distortions in measurements. Argonne had previously designed and tested shrouded sensors which create quiescent zones that enable undistorted measurements, but one drawback is the lower response time and the possibility of unrepresentative samples. To address these issues and provide optimized measurement capabilities that can meet challenging mass accountancy requirements, Argonne is developing flow-enhanced electrochemical sensors. The measurements from these sensors are based on the electrochemical response of electrodes immersed directly in the flow of the molten salt. This arrangement enables new potentiostatic and galvanostatic techniques which are less prone to noise in industrial environments due to the constant flux of salt at the electrodes.

To achieve flow conditions representative of molten salt reactor environments, Argonne constructed a testbed for the operations of FEES and other safeguards-relevant sensors. This system, known as the modular flow instrumentation testbed (MFIT), can accommodate a wide variety of interchangeable sensor test sections to permit the testing of the sensors under a variety of conditions and configurations. Initial molten salt operations with the MFIT began in FY21. In FY22 testing campaigns identified electrochemical waveforms useful for the determination of actinide concentrations and molten salt flow rates, and in FY23 the precision of the flow-enhanced sensors was improved. Deployments to an industrial partner institution also began in FY23. The objectives of FY24 were to test and optimize sensor measurements for very high-concentration salts that could be encountered in an MSR, improve sensor accuracy by leveraging multimodal sensors and new automation approaches, and continue sensor deployment activities in collaboration with partner institutions to demonstrate functionality in challenging real-world conditions.

This report summarizes the activities conducted during FY24. During this period, improvements to operations, sensor performance, and data analysis approaches were achieved. Sensors were also demonstrated in safeguards-relevant scenarios such as online salt purification. These combined activities are intended to help vendors achieve the regulatory requirements for material accountancy (10 CFR 74).

2. ELECTROCHEMICAL RESPONSE TO HYDRODYNAMIC CONDITIONS

As described in our earlier reports, flow-enhanced electrochemical sensors make use of hydrodynamic electrochemical approaches to measure the concentrations of species in the molten salt [9]. Electroanalytical methods for flow conditions require different electroanalytical approaches compared to quiescent conditions but can potentially offer several advantages. In quiescent conditions, a dynamic electrical signal is typically applied to the working electrode which results in a dynamic current response from the salt [2]. Flowing electrochemical sensors instead can operate using steady signals as the flow of salt provides a constant flux of analytes to the electrode surface. The use of steady signals eliminates several issues that can distort dynamic electroanalytical waveforms such as uncompensated resistance and kinetics effects.

Figure 1 shows a flow-enhanced electrochemical sensor design that can leverage the flowing salt to produce measurements of the concentrations of dissolved species within a molten salt. The sensor consists of multiple electrodes inserted into the process stream. Four main electrodes are used, including an upstream working electrode (WE1), two quasi-reference electrodes positioned downstream and lateral to the flow direction (REF1 and REF2), and a second working electrode directly downstream of WE1 (WE2). A fifth electrode or the transfer tube itself may be used as the counter electrode. A schematic of the third-generation FEES is shown in Figure 1. Compared to earlier designs, this implementation includes an extra insulator, fabricated from AlN-BN (Shapal), that is positioned axially along the transfer line.

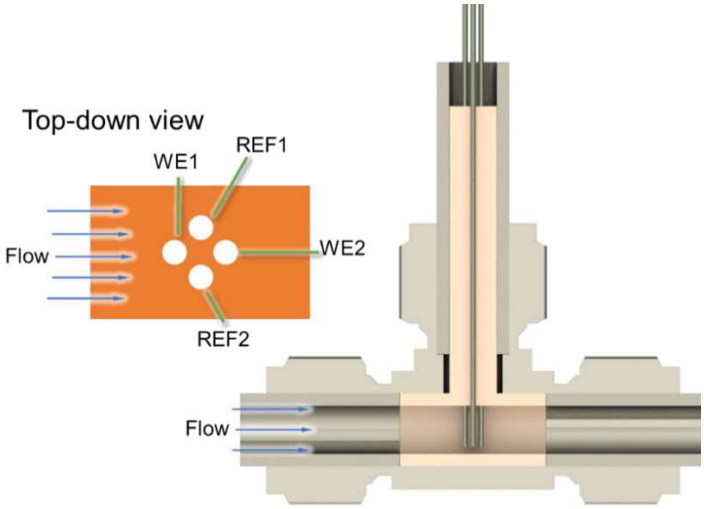

Figure 1. Schematic and rendering of sensor design in center section of MFIT transfer line [9].

Full details underpinning the mathematical modeling of these sensors is included in earlier work [9]. Ultimately, for soluble-soluble reactions such as U^{3+}/U^{4+}, the electroanalytical formulas that are used to convert measured currents into concentrations take the form

$$i = \beta Q^n \Delta C \qquad \text{Equation 1.}$$

$$\beta = \frac{(\pi/4)^{1-m} d D_i z F k S c^{1/3}}{\rho} \left(\frac{\rho}{\mu d_0}\right)^m \qquad \text{Equation 2.}$$

Here, F is Faraday's constant, z is the number of electrons associated with the charge transfer reaction, d is the electrode diameter, and M is molar mass of the species of interest, D_i is the diffusion coefficient of the species of interest, Sc is the Schmidt number of the dissolved species within the molten salt ($Sc=D_i/v$), ρ is the salt density, and k and m are values taken from mass transfer correlations associated with specific geometries. ΔC is difference in species concentration between the bulk fluid and the surface of the electrode. For limiting current conditions when the concentration at the electrode surfaces falls to zero, ΔC is equal to the bulk concentration of the species of interest. Similar formulas are possible for soluble-insoluble reactions [9].

A plot of the theoretical current response to an applied constant voltage is shown in Figure 2. The response contains a start-up period with either an upward ramp or a peak, depending on the specific parameters used for the applied signal. Eventually though, the current will reach its steady-state value. Current responses generated by these different applied signals offer multiple ways of determining the concentration of species within the salt. Ultimately though, the steady current output offered by the soluble-soluble approach offers higher quality measurements. For this reason, positive potential, soluble-soluble reactions have been the focus of our current efforts. The soluble–soluble response is particularly advantageous in that it avoids the electrode area growth that can compromise measurements and complicate calculations when using soluble-insoluble approaches.

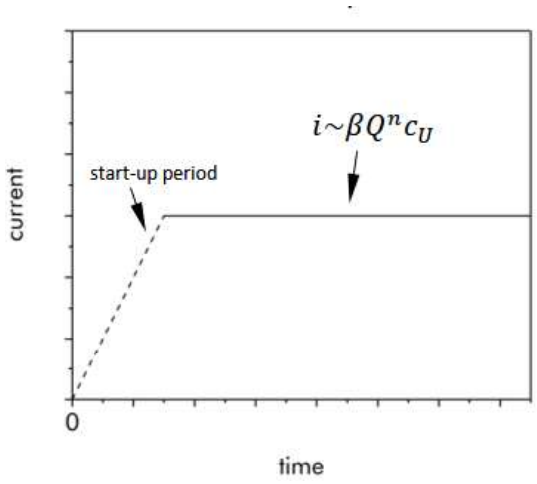

Figure 2. Theoretical current response for soluble-soluble reaction induced by applied positive potential [30].

Even with these advantages though, the FEES sensor approach has only been explored for relatively low concentration salts (up to ~5 wt% U). For MSR fuel salts, the sensor may need to be operated at much higher concentrations (> 50 wt% U), and improvements and optimization of the applied signals and analyses will need to be developed.

3. EXPERIMENTAL METHODS AND SETUP

Our activities in FY24 made use of two experimental apparatuses were constructed to support the development of the flow-enhanced electrochemical sensors (FEES) and other safeguards-relevant monitoring tools. Both systems are located within gloveboxes in a radiological laboratory at Argonne. These forced flow systems provide similar geometries for installation of FEES sensors but differ in the method of inducing flow. The first system, the Modular Flow Instrumentation Testbed (MFIT), uses a positive pressure differential to achieve high flow rates between 3 and 10 standard liters per minute (slpm). It can also accommodate radiological materials, such as uranium salts. The second system, the miniature-MFIT, is a scaled-down version which utilizes a negative pressure differential to achieve flow rates less than 2 slpm. The Miniature-MFIT leverages existing glovebox infrastructure and enables the salt composition to be more easily changed. This allows rapid changes of the flow system and its associated sensors to resolve design questions effectively. These systems were designed with careful consideration for operations, and numerous safety devices including relief valves, gas cut-off valves, a pneumatically actuated pressure relief valve, and a bubbler are included in the final construction. In FY24, both salt flow systems received a triannual safety review at Argonne.

A variety of transfer line diameters can be accommodated to create conditions representative of sampling lines, bypass lines, or the main coolant conduits on an MSR. The experimental results for MFIT systems in this report were conducted in a 0.5″ diameter transfer tube. Both MFIT systems include process and instrumentation software aimed at increasing repeatability, throughput, and safety of MFIT and FEES sensor operation. These features have allowed us to make hundreds of salt transfers over the past year without any significant operational issues.

3.1 MFIT System overview

The MFIT is forced convection molten salt flow system for evaluation of a broad array of sensors in actinide bearing molten salts. As shown in Figure 3(a), it consists of two vessels connected by a molten salt transfer line. The MFIT is installed in a glovebox, shown in Figure 3(b) which allows for large quantities of radiological salts to be used and enables rapid installation and modification of new sensor designs and configurations. Pressurized argon gas (<15 PSIG) is used to create the forced-flow conditions within the MFIT. This system was designed with careful consideration for operations, and numerous safety devices including relief valves, gas cut-off valves, a pneumatically actuated pressure relief valve, and a bubbler are included in the final construction. In FY24, the MFIT was operated with 2.1 kg of $MgCl_2$-KCl-NaCl-UCl_3 containing 3 wt % UCl_3. A flow-enhanced electrochemical sensor (FEES) is installed in the center of the transfer line. A multielectrode array voltammetry sensor (MAVS) is installed in one vessel. The MAVS makes measurements of uranium chloride and corrosion product concentrations and can measure the height of the salt relative to the sensor electrodes.

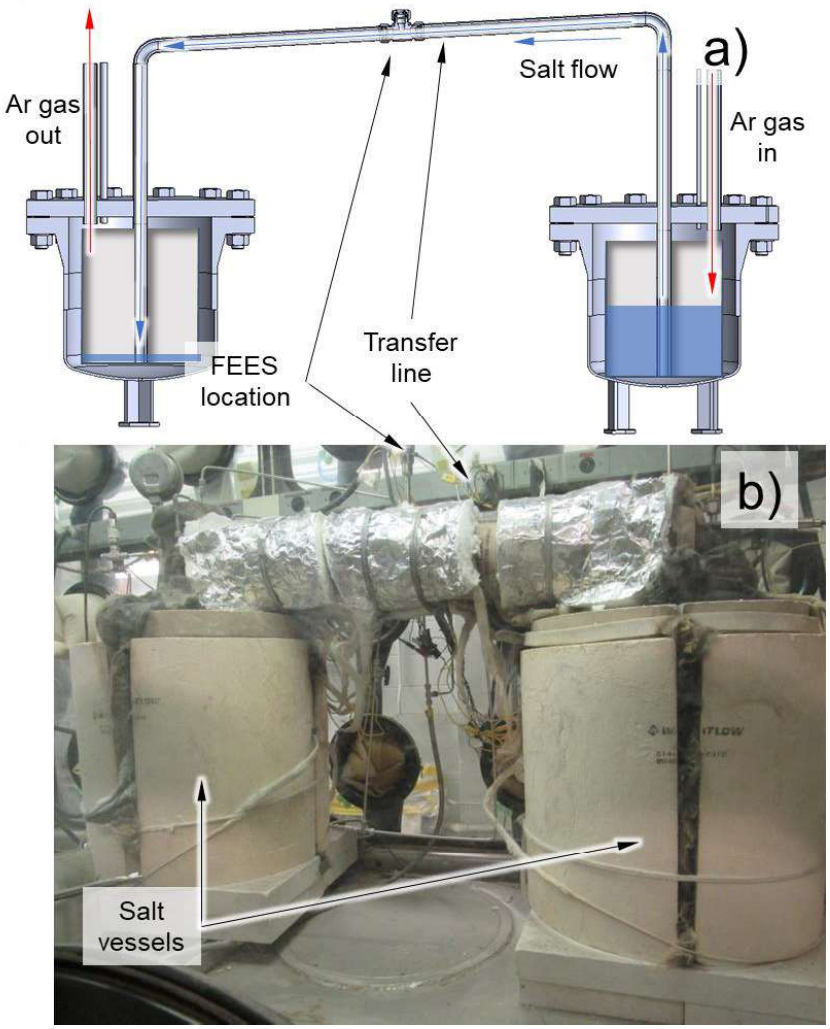

Figure 3. Pictures of (a) MFIT complete with heater assemblies, sensors and insulation installed into an (b) inert atmosphere glovebox [9].

3.2 Miniature-MFIT System Overview

The Miniature-Modular Flow Instrumentation Testbed (Miniature-MFIT) was designed and constructed in FY22 to study non-radiological salt systems and enable rapid vetting of new FEES and multimodal sensor designs [9]. Figure 4 shows the Miniature-MFIT (right) and its gas control system (left). The Miniature-MFIT is installed within an existing furnace well in a non-radiological glovebox at ANL as shown in Figure 5. The Miniature-MFIT consists of a salt holding tank, process tube, and salt reservoir. It applied a negative pressure differential between the salt holding tank and the reservoir to induce salt flow. A FEES was inserted into the flow path inside the dip tube. An additional level sensing electrochemical probe was inserted into the salt holding tank to monitor the level of the salt and provide an additional measurement of salt flow rate. A MAVS sensor is inserted into the salt reservoir to measure properties in quiescent salt conditions for comparison to the flowing salt data. This flow system can accommodate a maximum of 500 mL of salt which can easily be replaced or modified during testing.

In FY24, the system was operated with 500 mL of magnesium-contacted NaCl-KCl-$MgCl_2$ at 500 ˚C. Numerous multimodal electrochemical sensors and testing protocols were tested and vetted in the

Miniature-MFIT including multielectrode array level sensors (MALS) prior to deployment in radiological environments. The Miniature-MFIT was also an important development and testing ground for the ILEX Automation© software. This software has become an integral part of the MFIT capabilities enabling high-throughput semi-autonomous operation.

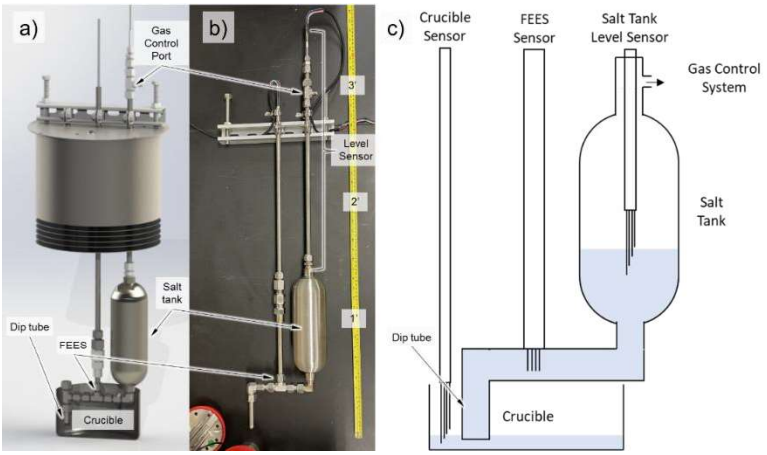

Figure 4. Mini-MFIT (a) rendering and (b) assembly without the furnace lid and (c) schematic of sensors and fluid flow path [9].

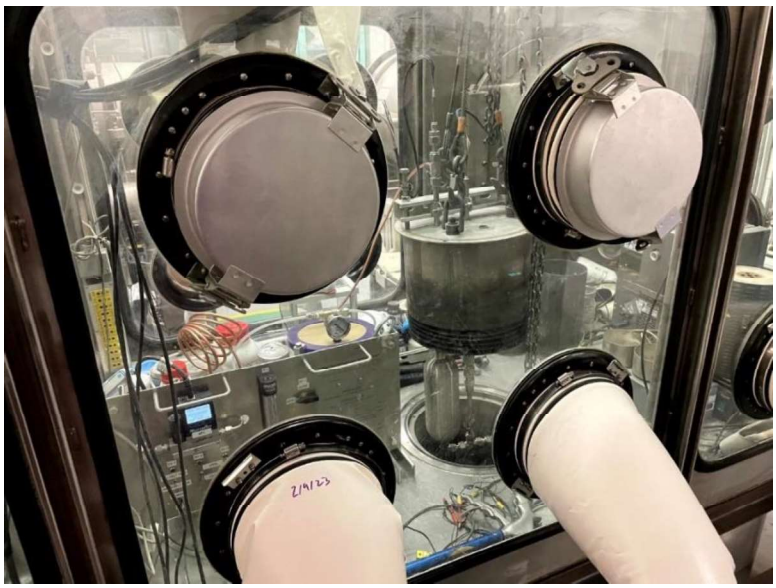

Figure 5. Gas control system (left) and Mini-MFIT system (right) installed in a non-radiological glovebox [9].

3.3 Monitoring Capabilities within the Modular Flow Instrumentation Testbed

The use of multiple sensors within the MFIT has helped to enable high accuracy real-time salt flow rate, salt level, and concentration measurements in support of FEES sensor assessments. This sensor suite also formed the technical basis for enhanced molten salt flow system predictive modeling. A list of currently installed sensors is included in the section below.

3.3.1 Flow-enhanced electrochemical sensors

The flow-enhanced electrochemical sensor currently installed in the MFIT has been in operation for over 12 months and has completed thousands of salt transfers. The sensor is robust and has tolerated numerous heating cycles when the MFIT was turned off for maintenance or to be reconfigured. Figure 6 shows a typical current response to a constant applied potential of 1 V vs. the tungsten quasi-reference electrode. This sensor setpoint was determined based on previous work in FY24. A FEES measurement has several features. When the potential is applied before the salt enters the transfer line, there is a small amount of current that decays as residual salt on the electrodes is reacted. When the salt contacts the FEES sensor there is an initial startup period associated with the instrumentation and the salt filling the transfer line. The current then reaches a plateau associated with the steady state current expected. Finally, the signal becomes noisy as gas is forced through the transfer line and salt flow ceases. To obtain flow rate from the FEES sensor, the flow duration is taken as the time between when the salt contacts the sensor and when gas begins to be forced through the sensor. Varying amounts of salt bubbling at the end of FEES measurements contributes to some error in the flow duration determination. The current response to the applied potential at a given flow rate is taken as the average of the flow duration. It should be noted that the use of process gas to drive flow and the geometry of the MFIT result in a siphoning effect that can alter the current response due to variation in the flow rate.

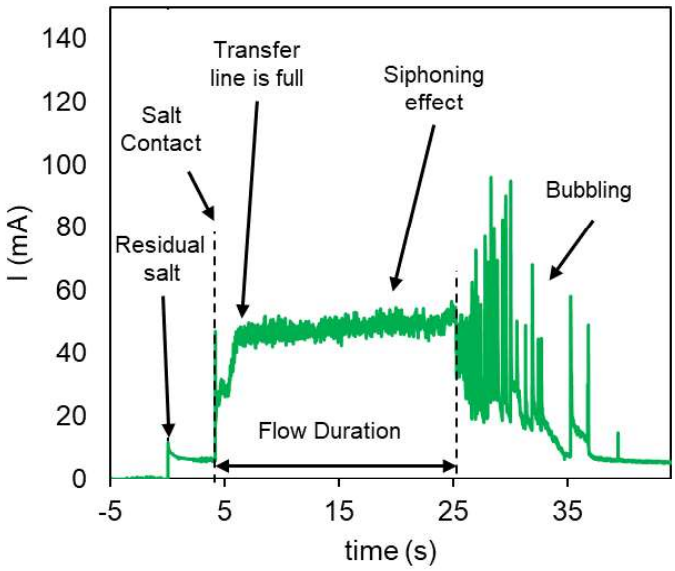

Figure 6. Flow-enhanced electrochemical sensor current response at a mass flow rate controller setpoint of 3 slpm.

3.3.2 Multielectrode array voltammetry sensors

Multielectrode array voltammetry sensors (MAVS) were deployed to facilitate actinide and corrosion product measurements. One advantage of a MAVS is the ability to self-validate key parameters, such as the electrode surface area in each experiment [2]. A Gamry Interface 5000E potentiostats is used for all voltametric and FEES sensor measurements. A Keithley 3700A System Switch with 10 Channel High Current Multiplexer cards is used to sequentially connect the potentiostats to the MAVS and FEES sensors. When combined with a multiplexer and programmed using ILEX Automation© software rapid measurements of salt chemistry and physical inventory are possible. The MAVS utilized in the Miniature-MFIT and the MFIT for radiological salts consisted of four 1 mm diameter tungsten electrodes that were positioned with a 5 mm stagger relative to one another. In the MFITs, the counter electrode is the vessel wall and the reference electrode is a tungsten quasi-reference electrode. For high concentration actinide salts a lower sensor surface area was desired to limit the current response from the highly concentrated species. The MAVS sensor for high concentration actinide salt measurements consisted of four 0.5 mm diameter tungsten electrodes that were positioned with a 3 mm stagger relative to one another. The reference electrode and counter electrode were a 2 mm tungsten electrode. The reference electrode was a 1 mm tungsten electrode. Comparison of the current response from each electrode enables near-real-time quantitative analysis.

3.3.3 Multielectrode array level sensors

In FY23, a new salt level sensor was designed and constructed for verification of fluid flow in the mini-MFIT. Independent knowledge of the flow rate is crucial for sensor calibrations and development of high-fidelity flow measurements using electrochemical sensors. Pictured in Figure 7, the salt level sensor consisted of a continuity measurement device connected to an array of electrodes space vertically in 5mm increments. As depicted in the diagram in Figure 7(c), the level sensor measured the continuity between the salt tank and the four electrodes in the sensor. When the salt touched an electrode in the sensor, a circuit between the electrode and the salt tank was completed by the salt. The continuity measurement device measured the voltage generated by the small current (<1 μA) which was allowed to flow between electrode and salt tank when the salt was touching the electrode. ILEX Automation© software was used to calculate the change in fluid level in the salt tank with respect to time. Flow rate measured by taking the change in fluid height and multiplying it by the cross-sectional area of the vessel. Figure 8 shows the salt level and fluid flow rate displayed in real-time. A linear curve fit gives the change in height with respect to time. The software can be calibrated for vessels of various internal diameters enabling the sensor to be deployed in a variety of testing conditions.

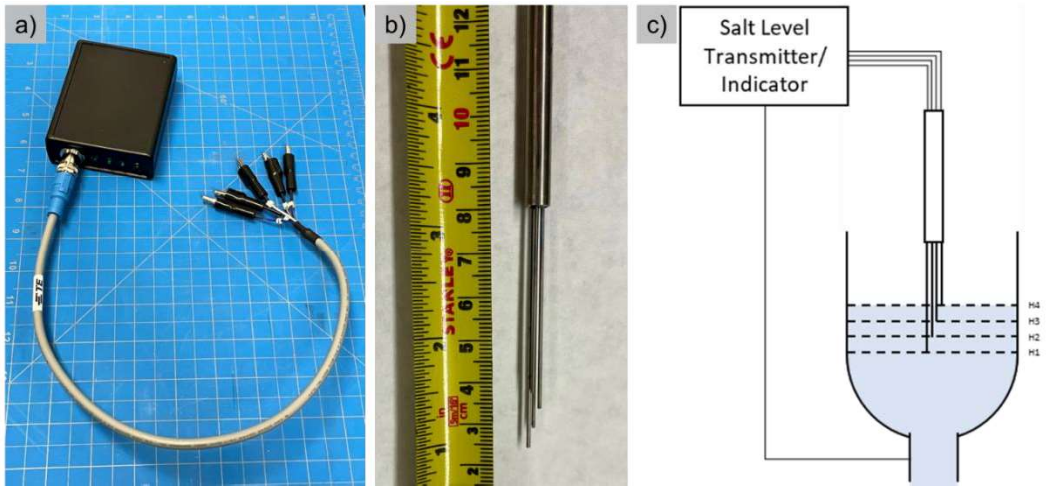

Figure 7. Mini-MFIT salt level sensor (a) continuity measurement device, (b) electrode array sensor, and (c) diagram of salt level sensor placement in the MINI-MFIT salt tank.

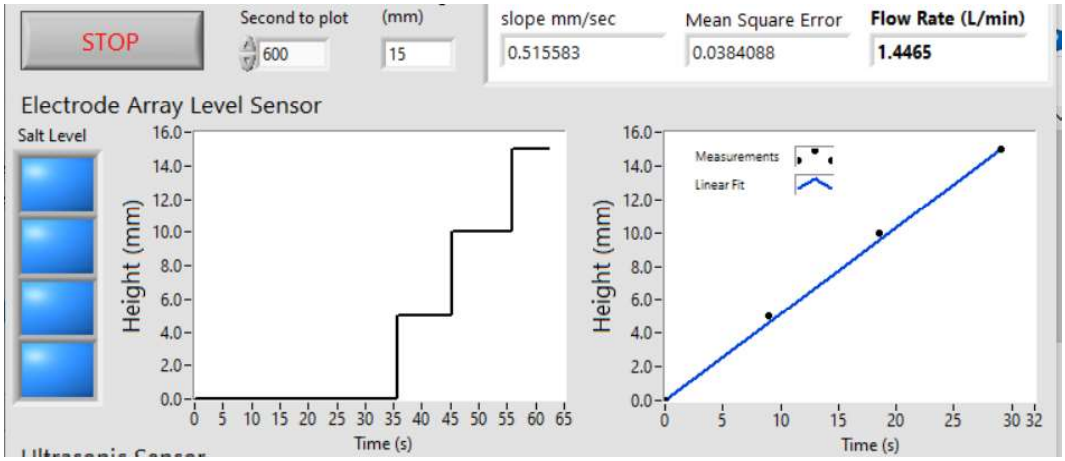

Figure 8. Multielectrode array level sensor (MALS) digital interface software.

3.3.4 Miscellaneous sensors

The full-scale MFIT is instrumented with an array of controls and sensors for process monitoring including, mass flow controllers, thermocouples, pressure transducers. Figure 9 depicts signals acquired during multiple salt transfers at various mass flow controller setpoints in the MFIT. Salt flow is induced by passing Ar gas at a set mass flow rate to pressurize vessel A or B. The pressure of the vessel containing the salt rises sharply until all the salt is transferred into the other vessel, then begins decrease. FEES measurements were conducted when the salt was transferred from vessel A to vessel B at a variety of flow rates. The temperature of the salt in vessel A and the FEES sensor were monitored with thermocouples. These sensors offer important diagnostic tools to ensure high-quality salt flow experiments and FEES sensor measurements.

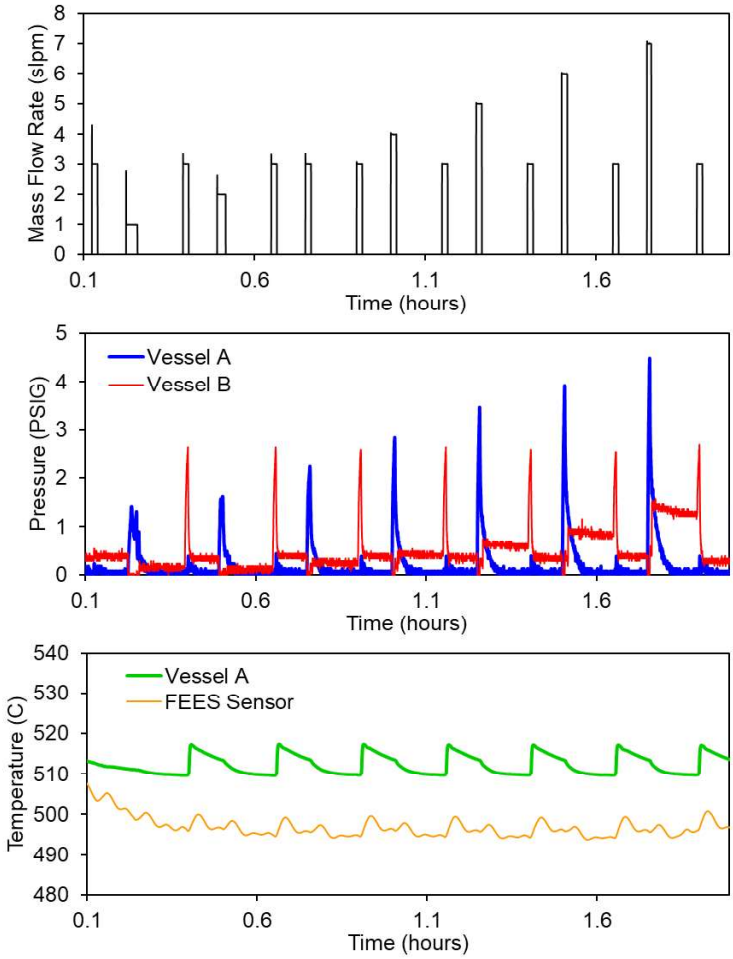

Figure 9. Modular flow instrumentation testbed mass flow controller, pressure transducer, and thermocouple measurements during multiple salt transfers at various mass flow controller setpoints.

Argonne is also developing and integrating several real-time salt level measurement capabilities to further improve flow rate measurement accuracy. These measurements help correlating phenomena, such as the salt siphoning effect, with FEES current response. An ultrasonic level sensor was built using off the shelf components for rapid technology evaluation. The ultrasonic level sensor, shown in Figure 10, consisted of a DFRobot URM14 200KHz Industrial Ultrasonic Distance Sensor inserted into a 19 mm OD 316 stainless steel tube 76 cm long. An ultrasonic sound pulse travels down the length of the tube and reflects off the fluid surface in the tube. The time delay between the sound pulse and measurement of the reflected sound is used to calculate the distance of the fluid surface from the sensor. Preliminary low-temperature ultrasonic level sensor testing in water was successful. The ultrasonic sensor was able to measure the fluid height to within ±0.3 mm. The advantage of the ultrasonic sensor over MALS sensors are improved salt level resolution and the ability to measure flow rate with a higher frequency. The sensor is being transitioned to the molten salt system, however, the robustness of the sensor in the extreme environment still requires further demonstration, and experimentation with these sensors is ongoing.

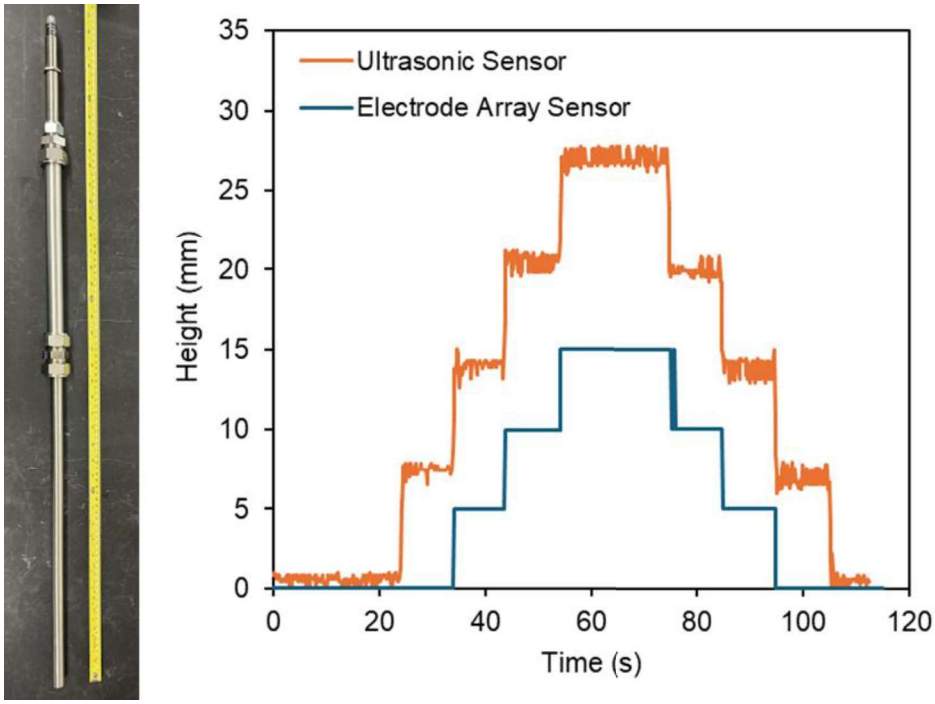

Figure 10. Comparison of ultrasonic level sensor and multielectrode array level sensor during incremental changes in water height of 7 mm at room temperature.

4. Assessment of FEES in High-Concentration Actinide Salts

Development of an effective and practical materials control and accounting (MC&A) capabilities is key to the licensability of MSRs within the United States. These capabilities are a challenge as there are a plethora of proposed fuel salt chemistries containing various quantities and types of nuclear materials, including low-enriched uranium (LEU), high-assay LEU (HALEU), thorium, and plutonium. Quantifying how these nuclear materials move through a nuclear facility, particularly for liquid fuel-salts that are not discrete items, is an engineering challenge that requires new robust and accurate sensors [10]. However, many of these reactor designs operate with very high concentrations of actinides, which complicates the operation of many of the proposed on-line and in-line monitoring tools [11]. FEES sensors could provide key measurements to support the safeguarding and accounting of actinides in MSRs, but to do so they must first be tested in very-high actinide concentration chloride salts. Our activities this year sought to establish these capabilities by investigating and optimizing operations of electrochemical sensors in LiCl-KCl-UCl_3(72 wt%) to ensure their continued performance across all MSR-relevant salts.

4.1.1 UCl_3 Measurements in High-Concentration LiCl-KCl-UCl_3

In FY24, electrochemical measurements were conducted in LiCl-KCl containing concentrations of UCl_3 as high as 72 wt%. This salt system is a useful analog for several proposed MSR fuel salts and shares similar behavior to NaCl-KCl-UCl_3 and NaCl-UCl_3. Linear sweep voltammetry (LSV) was the primary electrochemical technique used in this study as it enables investigations of salt composition measurements while providing thermodynamic and kinetic properties of the salt that are needed for proper FEES sensor operations.

The LiCl-KCl salt was synthesized from 99.9% pure components purchased from Noah Technologies Corporation. LiCl-KCl-UCl_3 with the nominal composition of 50 wt% depleted uranium (72.3 wt% UCl_3), shown in Figure 11, was previously produced via a cadmium UCl_3 production process [12]. The 72.3 wt% UCl_3 sample was diluted with the LiCl-KCl eutectic salt to obtain the nominal compositions of 60.8 wt% UCl_3 and 66.6 wt % UCl_3. Table 1 shows the composition of the LiCl-KCl eutectic salt and several compositions of LiCl-KCl-UCl_3 which were investigated in this study.

Figure 11. LiCl-KCl-UCl_3 (left) 72.3 wt% UCl_3 and (right) 60.8 wt% UCl_3 before and after electroanalytical experiments.

Table 1. Composition of LiCl-KCl and LiCl-KCl-UCl_3 salt mixtures for electrochemical studies.

Nominal Composition	UCl_3	KCl mol %	LiCl	UCl_3	KCl wt %	LiCl
Eutectic		41.8	58.2		55.8	44.2
50 wt% U	29.8	40.9	29.4	72.3	12.2	15.4
46 wt% U	24.4	44.0	31.6	66.6	14.8	18.7
42 wt% U	20.1	46.5	33.4	60.8	17.3	21.9

To demonstrate the feasibility of FEES sensor techniques at high-concentrations, a three-electrode array comprised of 0.5 mm diameter tungsten electrodes that were positioned with 3 mm axial staggering was used to examine the UCl_3/UCl_4 reaction. A comparison of the current response from each electrode enables near-real-time quantitative analysis. The counter electrode was a 2 mm tungsten electrode. The reference electrode was a 1 mm tungsten electrode.

Cyclic voltammetry was first performed on the salt as it is a useful tool to survey new chemical systems. Figure 12 shows CVs of the usable potential range of pure LiCl-KCl (58.2-41.8 mol %) and LiCl-KCl-UCl_3(66.6 wt %). At positive potentials the evolution of Cl_2 gas led to a large positive current curve. In LiCl-KCl, the usable potential range was bounded by the reduction of Li^+ to Li metal, a reaction that produced large negative currents due to the high concentration of Li^+ and rapid mass transport. As U^{3+} has a higher reduction potential than Li^+, the usable potential range was much narrower for LiCl-KCl with high concentrations of UCl_3. In these cases, uranium served as the lower potential limit due to the large cathodic currents associated with its deposition.

When the potential of the electrode immersed in LiCl-KCl-UCl_3(72wt%) was decreased from its resting potential only small currents were initially generated until the potential reached the U/U(III) reduction potential. Reversing the potential scan direction produced large positive currents as the U metal was re-oxidized into the solution. As the potential of the electrode was increased above its resting potential, though, large positive current peaks corresponding to the U(III)/U(IV) oxidation reaction were able to be observed. Very little current corresponding to the reduction of U(IV) was present in the initial negative potential sweep, indicating the U(IV) to U(III) ratio of the salt was very small. Comparison of the current generated upon the initial negative potential sweep and the final negative sweep after oxidation of U(IV) shows that the experiment creates a small amount of U(IV) locally near the electrode surface. In quiescent salt conditions, the U(IV) must be given time to diffuse away or back react before repeatable measurements can be achieved. However, it is unlikely that generation of U(IV) will negatively impact FEES sensor measurements because the electrode surface is constantly being replenished with fresh salt.

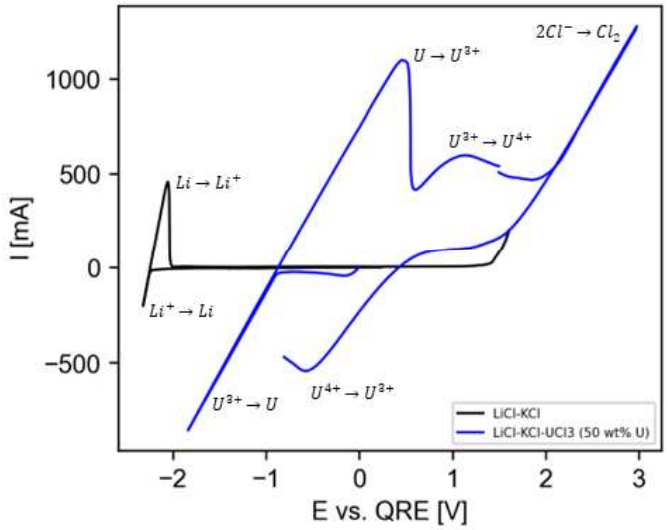

Figure 12. Cyclic voltammogram of LiCl-KCl and LiCl-KCl-UCl_3(60.8 wt%) at 600 ˚C.

Despite the large concentration of uranium, the current response of the U(III)/U(IV) reaction still exhibited a peak indicating that it was mass transport rate limited. This enabled application of conventional approaches for electrochemical measurement of high concentration U(III) in chloride salts. Several diagnostic criteria were examined to determine which electrochemical assumptions could be applied for quantitative analysis of voltammetry data. An electrochemical reaction in which the rate of electron transfer is fast is electrochemical reversible. For a reversible electrochemical reaction, the peak current is proportional to species concentration and is expressed by the Randles-Sevcik equation.

$$I_p = 0.446nFAC\sqrt{\frac{nF\nu D}{RT}} \qquad \text{Equation 3.}$$

Here n is the number of electrons transferred in the reaction, F is Faraday's constant, A is the surface area of the electrode, C is the concentration of the reacting species, ν is the potential scan rate, D is the reacting species concentration, R is the gas constant and T is the temperature. In Figure 13, LSVs at various potential scan rates were used to investigate the reversibility of the U(III)/U(IV) redox reaction. Figure 13(a) shows a single set of redox peaks corresponding to the oxidation and reduction of U(III) and U(IV). Several aspects of the results indicated that the reaction could be reversible. For example, the magnitude of the anodic and cathodic peak currents was comparable. Additionally, in Figure 13(b) the peak currents scaled linearly with the square root of scan rate. A few observations, however, indicated that application of the Randles-Sevcik equation would be problematic without additional corrections. Figure 13(c), for example, shows that the peak potentials are not independent of scan rate. The potential difference between the anodic and cathodic peak potentials was also much larger than the 57 mV expected for a reversible one-electron reaction.

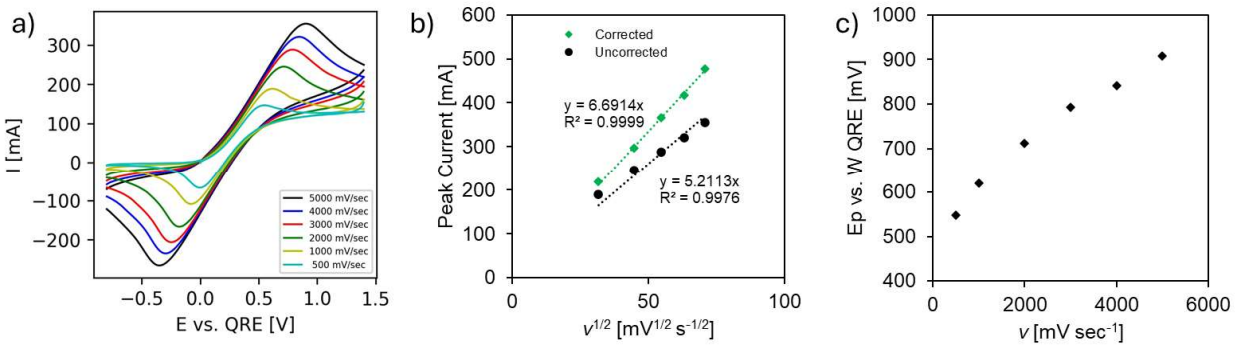

Figure 13. Cyclic voltammetry of LiCl-KCl-UCl_3(66.6 wt %) at 600 ˚C (a) at various potential scan rates, (b) the peak current vs. the square root of scan rate, and (c) the anodic peak potential at various scan rates.

Distortion of voltammetric responses is expected at very high concentrations [3]. Geometric effects, solution characteristics, migration, and other attributes may cause the distortion of potentiodynamic electrochemical data, such as the LSVs in Figure 13. Voltammetry can be affected by the presence of uncompensated resistance in the solution between working electrode and reference and by the interfacial capacitance of the electrode [13]. To correct for these effects, a subset of the possible non-idealities were addressed through the use of digital simulations.

Figure 14 shows simulations of the effects of uncompensated resistance on the voltammetry response from the salt. Uncompensated resistance modifies the effective scan rate and leads to peak broadening that can lead to difficulties in comparison of theory and experimental data [14]. While positive feedback *iR*-compensation is an experimental approach to account for solution resistance, feedback and oscillation that occur when large solution resistances are present limit the approach's practicality [15]. It is pertinent to note that while uncompensated resistance will affect dynamically changing signals like voltammetry, it will not affect constant potential measurements used by the flow-enhanced electrochemical sensors.

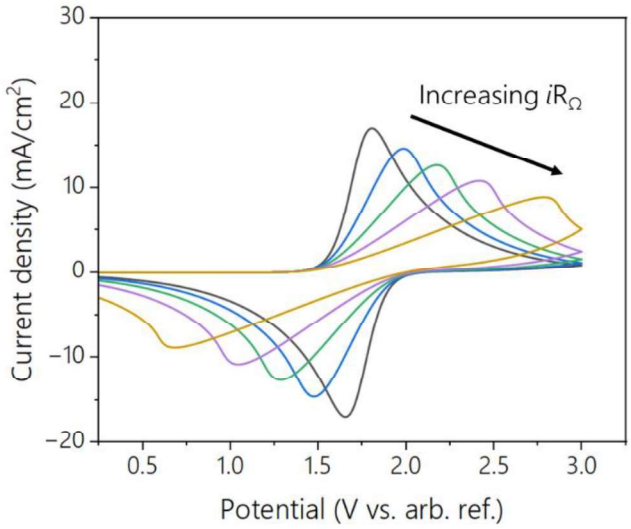

Figure 14. Simulated cyclic voltammograms showing the effects increasing solution resistance [16].

To improve accuracy of high concentration actinide measurements, the simulated results in Figure 14 were used to develop current multipliers to account for the depression of the peak currents [3]. The digital simulation assumed a highly concentrated species undergoing a one-electron reaction. The result of the simulation was an expression for the current multiplier, *CM,* needed to adjust for a given amount of peak depression in a voltammogram [16].

$$CM = -0.2858(E_p - E_{p/2})^2 + 1.3597(E_p - E_{p/2}) + 0.7797 \qquad \text{Equation 4.}$$

Here E_p is the peak potential (V), and $E_{p/2}$ is the half peak potential (V). Figure 13(b) shows that when the measured peak current density is multiplied by the current multiplier corrections, the peak current density becomes proportional to the square root of scan rate as is predicted by Equation 3.

With these corrections, the repeatability of cyclic voltammetry measurements was investigated to ensure sufficient accuracy for subsequent electrochemical studies in high concentration actinide salts. Figure 15 shows results therein using fast potential scan rates of 3000 mV/sec with the delay and re-equilibration steps required between measurements (5 minutes) to obtain repeatable results. The fast potential scan rate enables the measurements to be made quickly and minimize the generation of high concentrations of U(IV) at the electrode surface which may be volatile and or remain in the salt for long periods of time. The delay between LSVs allowed for the U(IV) produced in the positive anodic sweep to either diffuse away or be converted back to U(III). An open circuit potential following each voltammogram was recorded to observe the salt relaxation after each perturbation. In general, an open circuit potential of <10 mV was selected as the criteria to ensure that the salt had relaxed back to a repeatable uniform composition. In ten repeated measurements on the single electrode, the average anodic peak current density was 279 ± 4 mA. The consistency of the preliminary measurements on a single electrode boded extremely well for high accuracy measurement of actinides even at high concentrations.

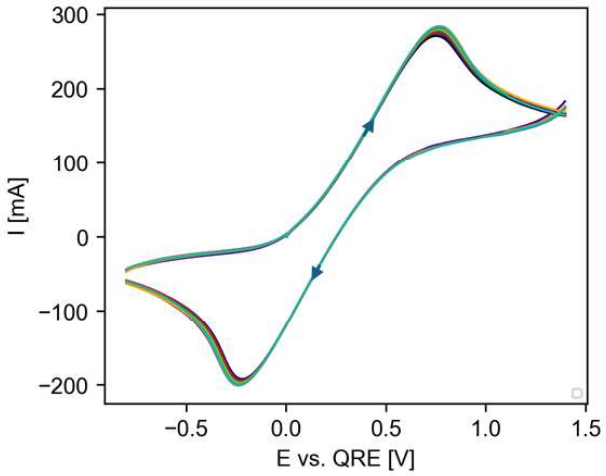

Figure 15. Ten repeated cyclic voltammograms of LiCl-KCl-UCl_3 (46 wt% U) at 600 ˚C. The potential scan rate is 3000 mV/sec and there is 5-minute delay between voltammograms.

Electroanalytical techniques used to obtain key parameters, such as electrode surface area, for species quantification were next evaluated. With a multielectrode sensor, the electrode surface area needed to parameterize Equation 3 can be obtained in near real-time [2]. Figure 16(a) shows LSVs recorded on the three electrodes with a 3 mm difference in submerged length in LiCl-KCl-UCl_3(66.6 wt %). For each

electrode, measurements were recorded in triplicate with the same protocols used in Figure 15. Plotting the anodic peak current as a function of the change in height of the electrode from the deepest electrode, the length of the electrode that was submerged in the salt could be extrapolated in Figure 16(b). Using these values the respective surface areas of each electrode, correlations between peak current density and species concentration could be made using Equation 3. Figure 16(c) demonstrates how the LSVs can be normalized to account for electrode surface area. Small differences in the peak spreading of LSVs obtained on each electrode were indicative of differences in uncompensated resistance dependent on the electrode depth.

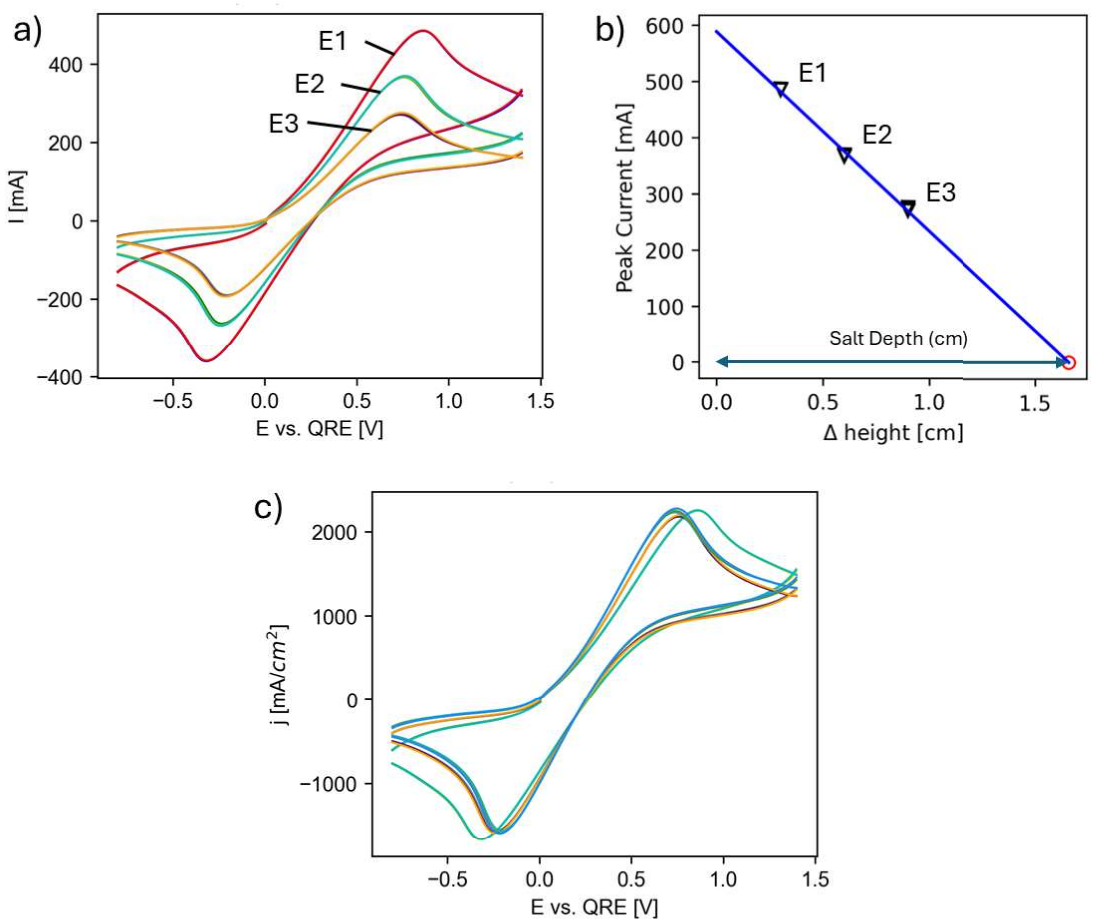

Figure 16. Linear sweep voltammetry of LiCl-KCl-UCl_3(66.6 wt %) at 600 ˚C using a multielectrode array voltammetry sensor (MAVS) to (a) obtain the current response from each electrode (in triplicate), (b) determination of electrode surface area from the anodic peak current, and (c) all cyclic voltammograms after surface area correction. Potential scan rate is 3000 mV s^{-1}. The counter electrode is a 2 mm tungsten rod. The reference electrode is a 1 mm diameter tungsten quasi-reference electrode (QRE).

The average anodic peak current density corresponding to the oxidation of U(III) to U(IV) on each electrode was measured for each of the three salt compositions. Peak current densities were corrected using the appropriate current multiplier for peak spreading observed in each CV. The results for measured and corrected peak current density are shown in Figure 17. As shown, the corrected peak current values followed a proper trend with respect to concentration while the uncorrected values did not.

Analysis of the results indicated that the salt composition measurements at high U concentrations showed a relative systematic error of 4.7% (absolute error 2.2 wt%). The systematic error combined with the random error (1.3%) is higher than what had historically been observed in lower-concentration salts. Additional work to understand the source of these errors is being investigated, and improvements to the electrochemical cell and procedures are being adopted in an attempt to reduce the error to a more typical range.

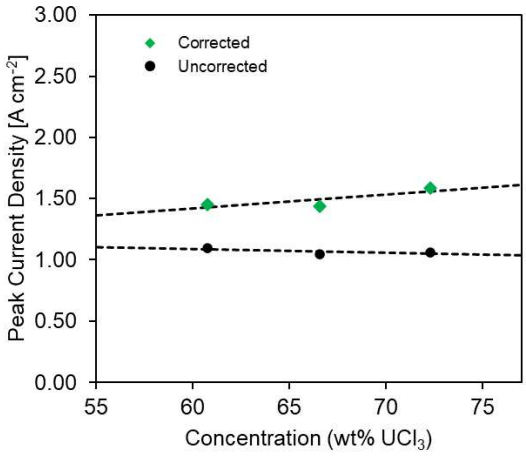

Figure 17. Peak Current density vs. UCl_3 concentration in LiCl-KCl-UCl_3 determined with a multielectrode array sensor at 600 ˚C.

Overall, the results of electrochemical sensor testing in high concentration actinide salts are promising and indicative of how FEES sensors will perform in flowing salt environments. All results so far have indicated that the oxidation of U(III) to U(IV) is a well-behaved reaction that enabled the application of electroanalytical practices, albeit with the necessity for digital simulations to correct for nonideal phenomena. Using potentiodynamic techniques, electrochemical cell geometry effects, such as interfacial capacitance and uncompensated resistance, will be considered to more accurately translate the salt's current responses into quantitative actinide concentrations. Potentiostatic techniques such as those used for FEES sensors, however, will not be susceptible to many of these effects; as such, the correction factors needed for FEES operations will be smaller than those used above.

4.1.2 High-Concentration UCl_3 Salt Production

Preparations for full testing of FEES sensors in flowing salts is underway, starting with salt production. To make the roughly 2 L of salt needed for testing in the MFIT, a reaction pathway for production of high uranium concentration NaCl-UCl_3 salt was investigated in FY24. The targeted salt was the NaCl-UCl_3 eutectic (65.9-34.1 mol %), which is a candidate molten salt fuel salt for MSRs. The goals of initial studies were to investigate feasibility, identify potential engineering challenges, and develop design criteria for a system to produce large quantities of this salt.

Several reaction pathways have been demonstrated for producing NaCl-UCl_3 mixtures from uranium metal. Molten salts for uranium electrorefining can be synthesized using $PbCl_2$ [17] and $CdCl_2$ [18], however these compounds pose significant safety and disposal challenges. $CuCl_2$ [19] and NH_4Cl [20] have been investigated produced high concentrations of UCl_4 which may corrode structural metals. $BiCl_3$ can produce actinide chlorides but possess a high vapor pressure at the process temperature making the reaction difficult to control [21]. Lee et al. [22] and Rose et al. [23] have chlorinated depleted uranium metal by reacting it with $ZnCl_2$ in molten salt LiCl-KCl both chemically and electrochemically. Zhang et al. [24] produced NaCl-UCl_3 (12 wt % U) by reacting a uranium rod with a molten salt mixture of NaCl and $FeCl_2$. Sakamura et al. [25] reposted chlorination of UO_2 using ZrF_4. One or a combination of these reaction pathways may be required to process uranium metal bearing compounds into usable MSR fuel.

The $ZnCl_2$ exchange reaction in an NaCl-$ZnCl_2$ solution was chosen for preliminary small-scale depleted uranium chlorination experiments. The exchange redox reaction between Zn and U metal to form UCl_3 (1) has a negative Gibbs free energy of reaction.

$$3/2\,ZnCl_2 + U \rightarrow UCl_3 + 3/2\,Zn \;\; (\Delta G = -238.3\,kJ\;at\;500\,^{\circ}C) \qquad \text{Equation 5.}$$

The reaction in which $ZnCl_2$ reacts to form UF_4 (2) is also thermodynamically favorable.

$$2ZnCl_2 + U \rightarrow UCl_4 + 2Zn \;\; (\Delta G = -187.3\,kJ\;at\;500\,^{\circ}C) \qquad \text{Equation 6.}$$

The formation of UCl_4 can be suppressed by contacting the salt with an excess of uranium metal [22]. The resulting Zn metal can be volatilized at high temperature and removed by reacting it with copper metal to produce brass.

Preliminary small-scale depleted uranium chlorination experiments were carried out in a furnace inside of an inert atmosphere glovebox which maintained the levels of moisture and oxygen below 5 ppm. Figure 18 shows the small-scale chlorination experiment. NaCl (99%) and $ZnCl_2$ (98%) obtained from Sigma-Aldrich were mixed and melted in a graphite crucible, shown in Figure 18(a). The composition of the initial NaCl-$ZnCl_2$ mixture is shown in Table 2. The molar ratio was such that there is a slight excess of $ZnCl_2$ to intentionally produce a salt that is rich in UCl_3. After melting in the graphite crucible there were some graphite particles initially present in the NaCl-$ZnCl_2$ mixture. The salt was then contacted with a depleted uranium ingot shown in Figure 18(b) at 500 ˚C for 12 hours. Following the reaction, the ingot was retrieved. The salt and ingot are shown after reaction in Figure 18(b) and Figure 18(d), respectively. The salt took on a dark color, and the ingot showed significant mass loss. It was estimated based on the mass loss of the ingot that the reaction had proceeded to at least 82 % completion. The salt was then heated to 700 ˚C to encourage the volatilization of Zn metal. Figure 18(e) and (f) show the discoloration in a copper mesh that was inserted into the furnace above the salt due to reaction with Zn vapor before and after processing.

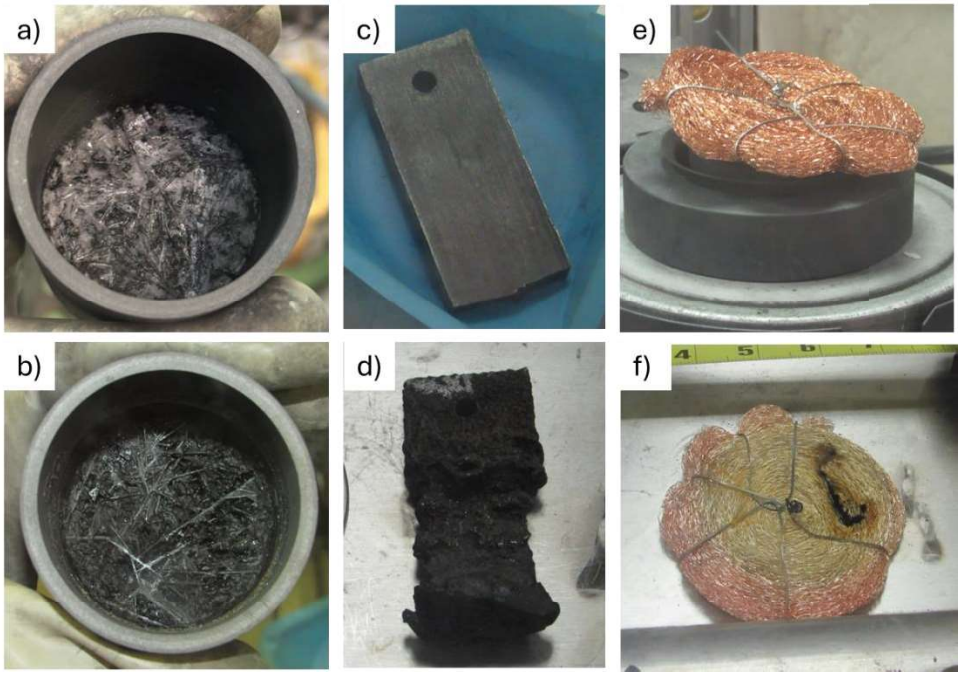

Figure 18. Images of a) the NaCl-$ZnCl_2$ and b) the resulting NaCl-UCl_3 from the uranium chlorination experiment. The depleted uranium ingot c) before and d) after reaction with $ZnCl_2$ and the copper mesh e) before and f) after reacting with Zn vapor.

Table 2. Composition of the initial NaCl-$ZnCl_2$ salt mixture.

	Mol %	Mass of Salt (g)
$ZnCl_2$	0.70	90.18
NaCl	0.30	38.65

Complete characterization of the NaCl-UCl_3 produced in this experiment was begun but will be completed in early FY25. Key initial findings will influence salt production methods going forward. Thus far, the procedure worked reasonably quickly, but issues such as the formation of U-Zn alloys and contamination from the graphite crucible have led to procedural changes for the scaled-up system [26]. Additionally, it was observed that the volatilization of Zn should be done quickly with adequate engineering controls to prevent spread to undesired locations in the glovebox.

To support full-scale production, Argonne National Laboratory reallocated an inventory of >30 kg of depleted uranium mesh powder to produce the research grade, high concentration actinide molten salts. The depleted uranium, shown in Figure 19, remained from previous uranium metal studies at Argonne and had been carefully stored in sealed containers under argon gas. The mesh powder is a more consistent and flexible alternative to uranium ingots and uranium dendrites recovered from electrorefiner activities. The powder can be shaped or processed in to more versatile geometries that can enable efficient chlorination in UCl_3 productions systems. Processing of the depleted uranium is scheduled to commence in early FY25.

Figure 19. Depleted uranium powdered mesh obtained from storage within an inert atmosphere container.

5. FEES Sensor Performance Improvements and Multimodal Monitoring

In FY24, additional performance improvements for FEES sensors were explored via integrated operations with other sensors for measuring fluid flow rate and species concentration. These complementary measurements proved able to improve measurements of the FEES themselves. These capabilities were first tested in the non-radiological mini-MFIT and then transitioned to the MFIT containing $MgCl_2$-KCl-NaCl with 3 wt.% UCl_3.

5.1 Multimodal Sensor Development in the Miniature-Modular Flow Instrumentation Testbed

The Miniature-MFIT enabled validation of new sensor technologies and automation capabilities without the costs associated with radiological operations. Two sensors, a MAVS and MALS, and methods for integrating them with FEES sensor measurements were developed in FY24. The MAVS and MALS were tested in $MgCl_2$-NaCl-KCl at 500 ˚C to measure impurity concentrations and fluid flow rate respectively. New functionalities were also added to ILEX Automation© software to enable automatic control of the MAVS sensor and flow rate calculations using data provided by the MALS sensor.

The performance of FEES in low flow rate regimes and low corrosion product concentrations was investigated with the Miniature-MFIT, as this was one region where the full-scale MFIT could not provide coverage. As part of this testing, a MAVS sensor was positioned in the Miniature-MFIT's salt reservoir where it could measure the salt composition in the quiescent salt in between flow tests. Figure 20 shows cyclic voltammograms from each MAVS electrode during these measurements of the salt within the crucible. ILEX Automation© was used to take sequential measurements on each MAVS electrode, a task previously done manually. Analysis of MAVS data was automated using Python analysis scripts to (1) obtain the submerged depth of the sensor in the salt, (2) quantify the redox potential of the salt, and (3) calculate the concentration of species in the salt utilizing peak current density. After several days of exposure to the mini-MFIT's structural materials (composed of 316L stainless steel), the chloride salt showed pairs of redox peaks corresponding to the reactions Cr/Cr(II) and Fe/Fe(II).

The inset plot in Figure 20 depicts the use of the reduction peak current to extrapolate the sensor submerged depth in the salt using the relative lengths of the MAVS electrodes. The concentration of Fe^{2+} was measured using the reduction peak current density, the Berzins-Delahay equation,

$$I_p = 0.6105AC\sqrt{\frac{(nF)^3 vD}{RT}} \qquad \text{Equation 7.}$$

and the Fe^{2+} diffusion coefficient of 9.16 x 10^{-6} cm^2 s^{-1} [27]. In this manner, the concentration of Fe^{2+} was measured to be 47.7 ± 0.5 ppm.

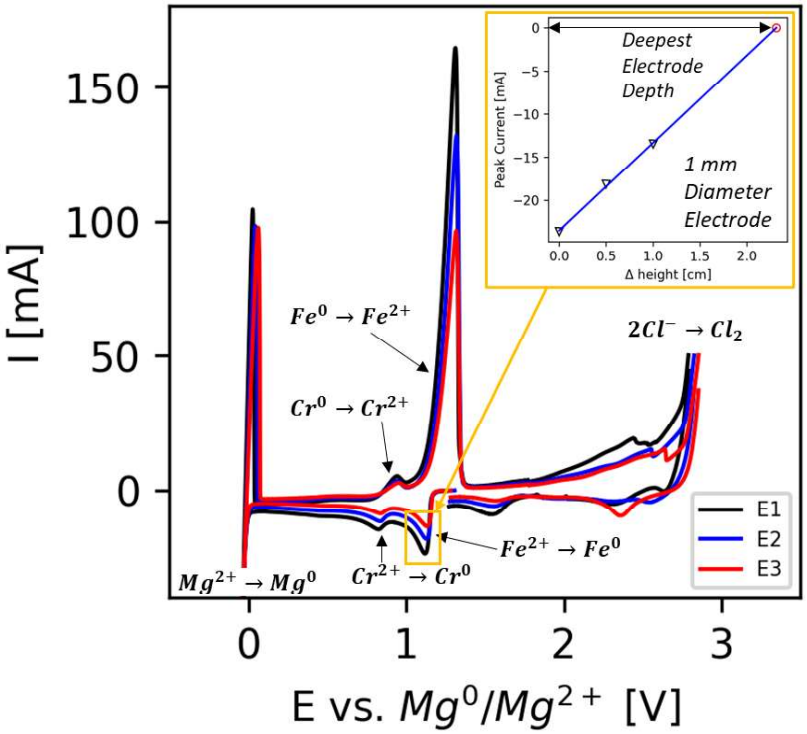

Figure 20. Cyclic voltammogram of stationary NaCl-KCl-$MgCl_2$ with corrosion products at 500 °C using a multielectrode array voltammetry sensor (MAVS).

The MALS was first demonstrated in the Miniature-MFIT. As shown in Figure 4, the MALS level sensor was positioned within the salt tank. ILEX Automation© and the Miniature-MFIT's gas control system carried out sequential salt fill and drain cycles at various salt flow rates between 0.05 slpm and 1 slpm. Figure 21 shows an example sequence of fill and drain cycles at various flow rates and the corresponding vacuum system pressure. A comparison of the measured salt flow rate obtained with the MALS sensor to the vacuum system mass flow controller setpoint is shown in Figure 22. There is good agreement between the measured salt flow rate and the setpoint indicating that this method of inducing salt flow is quite accurate. The slight deviation of the data from the parity line may have two possible explanations: (i) the internal diameter of the salt tank may have been different than the part drawing or (ii) the temperature of the Ar gas entering the mass flow controller may have been lower than the temperature of the gas in the MFIT, leading to a discrepancy in the setpoint and the actual mass flow rate. Nonetheless, the differences in measured flow rates were minor. With an online measurement of salt flow rate for each fill and drain cycle, accurate determination of the relationship between FEES sensor current response and species concentration can be made. The improved accuracy of the flow rate measurement, in turn, lead to improved measurements from the FEES sensor.

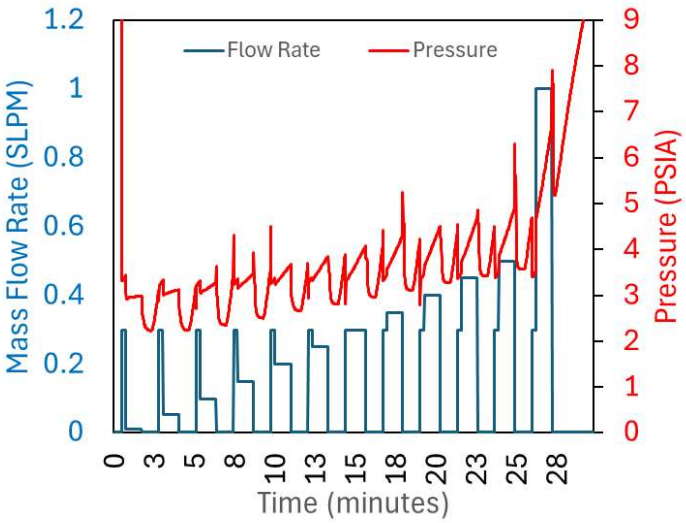

Figure 21. Miniature-MFIT gas control system Ar gas mass flow rate and vacuum pressure during salt flow tests at various mass flow rate flow rate setpoints.

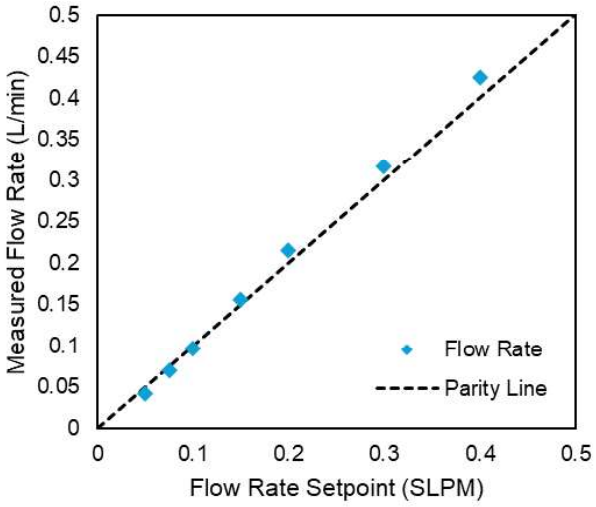

Figure 22. Miniature-MFIT multi-electrode array level sensor (MALS) flow rate measurements of NaCl-KCl-MgCl2 at 500 ˚C.

As a first demonstration of measurements combining information from the FEES and from the MALS level sensor, measurements of Fe^{2+} corrosion product in the mini-MFIT salt were conducted. Toward that end, Figure 23 shows the FEES current response to an applied potential of 2.2V vs. Mg/Mg^{2+} at salt flow rates between 0.01 and 1 slpm. Based on the results in Figure 20, the applied potential was sufficient to oxidize Fe^{2+} to Fe^{3+} producing positive currents. As the flow rate was increased, there was a transition between mass transport limited current response to the constant current response expected from Equation 1. Between 0.1 and 0.2 slpm the current response became relatively constant with respect to time with some added noise thought to be due to turbulent effects in the process stream.

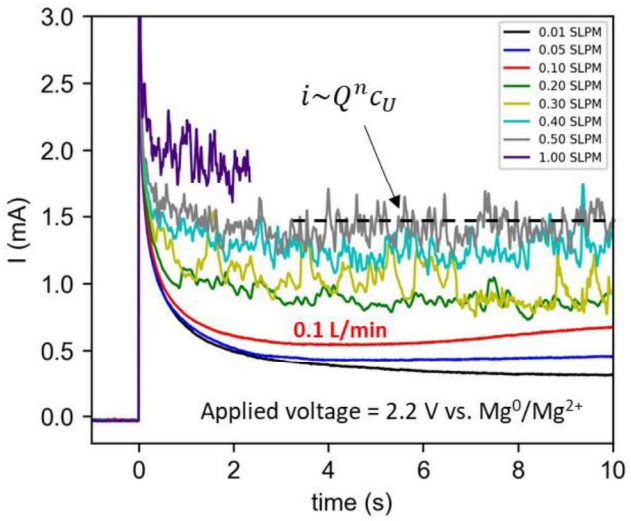

Figure 23. Current response to an oxidizing voltage in flowing NaCl-KCl-$MgCl_2$ with corrosion products at 500 °C.

The FEES current response was calculated by taking the average current recorded 2.0 seconds after the potential was applied to allow for the measurement to stabilize. Figure 24 shows this average current response at various flow rates measured using the MALS. The oxidation of Fe^{2+} was observed to increase non-linearly with flow rate as was expected by the mass transfer correlation, indicating that the sensor response scale appropriately down into this low-flow regime. Following the successful demonstration of the MALS in these non-radiological chloride salt experiments, the MALS was then deployed in the MFIT with dissolved UCl_3.

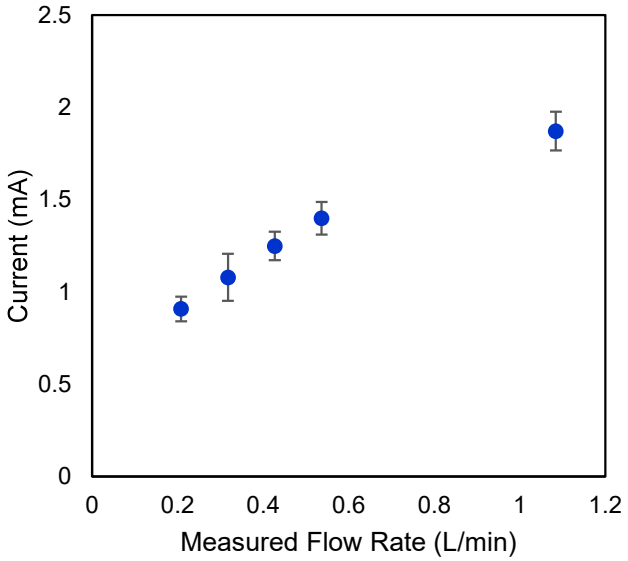

Figure 24. FEES average current response to constant applied potential during Miniature-MFIT salt flow at various flow rates.

5.2 Multimodal Sensor Development in the Modular Flow Instrumentation Testbed

A challenge for flow-enhanced electrochemical sensor analysis is accurate determination of salt flow rate in the MFIT. In previous work, flow rate was determined by dividing a constant change in salt volume by the measured length of time that the sensor's current response was steady before salt finished flowing across the sensor. Figure 6 shows a typical current response from the FEES sensor at an applied potential of 1V vs. reference under these assumptions. Here, the flow duration was calculated by assuming the salt volume transferred was the total volume minus the volume of salt held up in the bottom of the vessels. The measured length of time that the salt flowed across the sensor was affected by both the sensor startup period and the amount of gas bubbling that occurs in the transfer line at the end of each transfer.

However, issues with these flow rate measurements have been discovered to cause increased, spurious error for the FEES sensor's concentration measurements. For example, during FY24 over 120 salt transfers and FEES sensor measurements were made in 2.1 kg of $MgCl_2$-KCl-NaCl-UCl_3 containing 3 wt % UCl_3. Mass flow controller setpoints between 1 and10 slpm were used to gather statistical data over a broad range of flow conditions. Figure 25(a) shows that there is significant variability in the measured flow rate from the FEES sensor at each mass flow controller setpoint. Figure 25(b) in turn shows the current response of the FEES sensor is relatively stable at each mass flow controller setpoint but that there is variability in the flow rate measurements derived from the FEES sensor. Improvement in the accuracy of composition measurements from the FEES sensor therefore is dependent on the development of new multimodal sensors that can provide more accurate salt flow rate data within the MFIT.

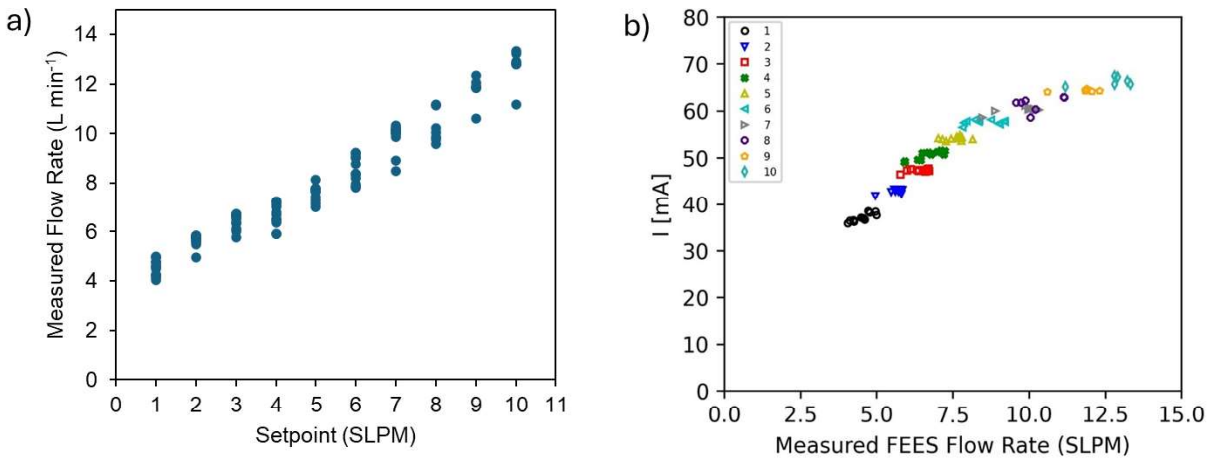

Figure 25. Flow-enhanced electrochemical sensor current response as a function of a) mass flow controller setpoints and b) FEES sensor flow rate measurements at each mass flow controller setpoint in standard liters per minute.

A MALS level sensor was therefore deployed to measure flow rate in one of the MFIT's salt vessels to improve FEES sensor accuracy. The results of MALS sensor measurements taken at 1 to 6 slpm are shown in Figure 26. The results show that the flow rate in the MFIT linearly increased over the range investigated. The difference in flow rates measured by the mass flow controller and by the MALS was likely due to process gas compressibility and the MFIT siphoning effect. A linear regression of the data showed relative standard error of 0.1 slpm. This regression was then used to calculate the theoretical salt flow rate at each setpoint used. Figure 27 shows the FEES sensor current response with respect to these independent flow rate measurements; the data using the MALS flow rates show much tighter grouping than the data using the FEES measurement. This suggests that independent flow rate data from the MALS should be used in concert with the FEES current response data to provide the best concentration measurements.

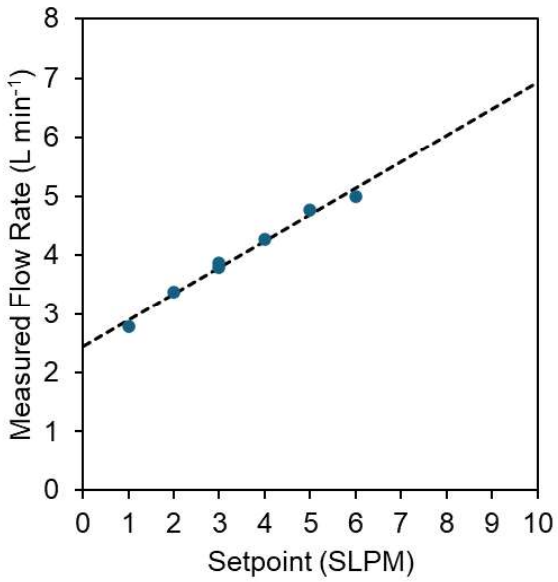

Figure 26. Multielectrode array level sensor (MALS) measured flow rate vs. the mass flow controller setpoint.

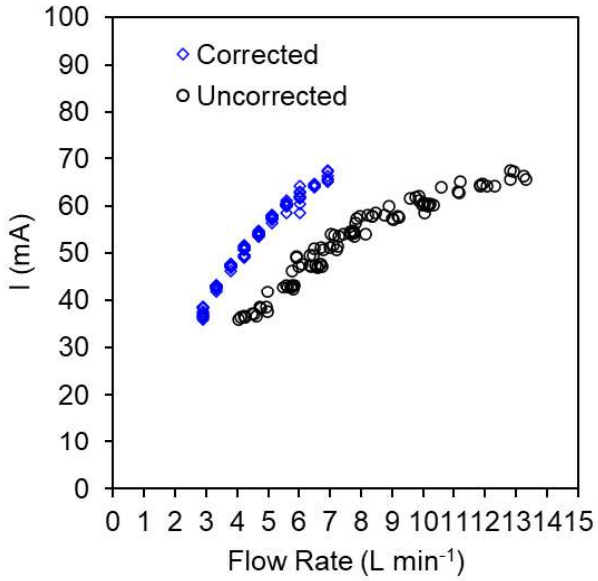

Figure 27. Flow-enhanced electrochemical sensor current response various flow rates. The uncorrected data is plotted against flow rates measured using the FEES sensor. The corrected data is plotted against flow rate measurements using the multielectrode array level sensor (MALS).

Having observed that FEES sensor current response is better correlated with the flow rate obtained from the independent MALS sensor, data previously recorded in FY23 was recalibrated to improve the predictive model for uranium concentration. For this analysis, it was assumed that no change in the hydrodynamic properties of the salt had occurred in the past year that would change the relationship between mass flow controller setpoint and MALS sensor measurements.

Accordingly, Figure 28 shows the FEES current response at various flow rates measured with the MALS sensor for concentrations between 0.5 wt% and 3.0 wt% UCl_3. The datapoints are averaged over ten transfers. Using this new data, a new non-linear surface fit was performed using the equation developed in FY22 (Equation 1). The result of the surface fit for parameters β and n are shown in Table 3. In Figure 28, the new curve fits of Equation 1 are represented by solid lines. Overall, the model equations are still well correlated across the concentration considered, although the model overpredicts the FEES sensor response for 0.5 wt% U. The origin of the differences at low concentration was discussed in our FY23 report, and the discrepancies at that concentration are likely due to residual impurities in the salt reacting with the UCl_3. This 0.5wt% data was accordingly omitted from the statistical analyses, as had been done previously [9].

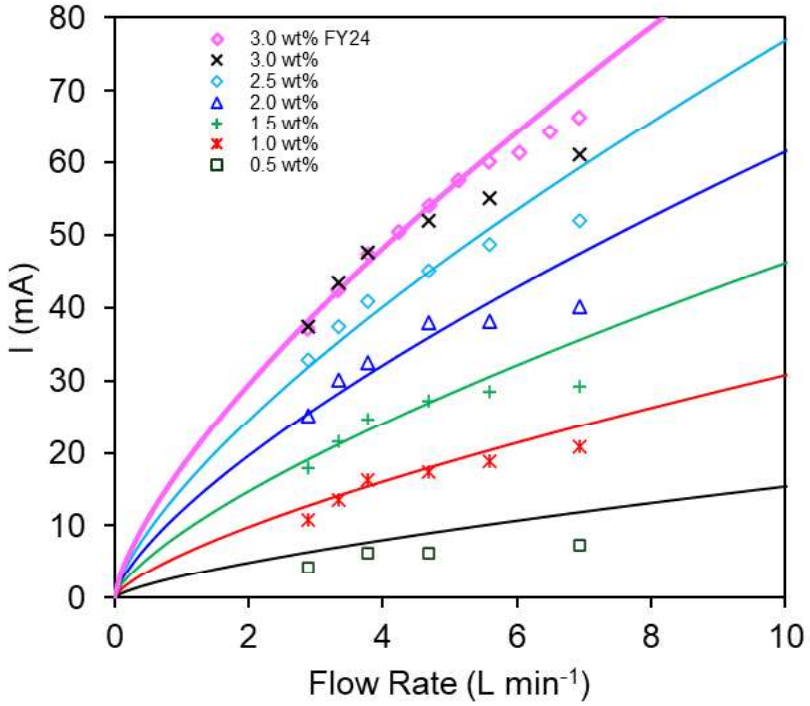

Figure 28. Flow-enhanced electrochemical sensor current response at different U^{3+} concentrations and flow rates. Lines represent the nonlinear-surface fit for the sensor response function.

Table 3. Updated Sherwood number parameters for FEES

Sherwood Number Parameter	FEES Correlation
β	6.0
n	0.71

Recalibration of the FEES data with the MALS sensor flow rate measurements led to a significant improvement in FEES sensor accuracy. Using the new Sherwood number parameters, the concentration of UCl_3 was calculated for all UCl_3 concentrations measured in FY23 and FY24. Figure 29 shows a parity plot of the measured uranium concentration versus process knowledge analyzed in this way. The U concentration data measured in FY24 across a range of flow rates for salt with a known concentration of 3 wt% UCl_3, as represented by the green triangular datapoint, generated predicted concentrations of 2.96 ± 0.08 wt% with a relative standard error of 1.6%. Across the full range of old and new measurements, the FEES data showed an improvement in the mean absolute relative error of 2.5% compared to 3.1% in FY23.

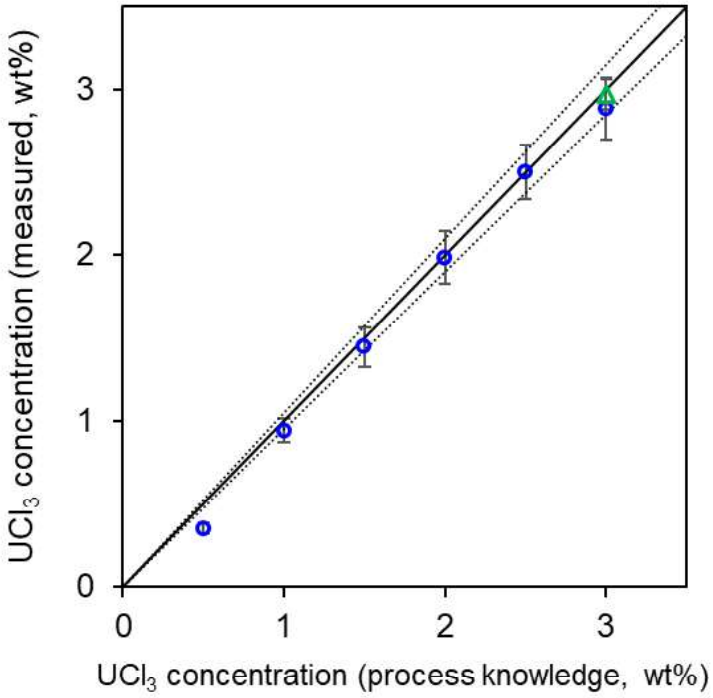

Figure 29. Parity plot of uranium concentration from process knowledge and uranium concentration measured across a full range of flow rates using the FEES.

6. Multimodal Monitoring Demonstration During Complex Flow System Operations

The presence of online salt processing systems is often cited as a safeguards concern for MSRs [10]. The salt processing procedures typically involve the addition of reactive metals (e.g., Be metal, uranium, metal, etc.) to control the salt redox potential and remove corrosion products and impurities [28]. Other methods of salt processing are also possible. Regardless of the approach, the transfer of fuel salt into a piece of equipment where its composition is altered poses challenges for material accountancy [29]. To provide a preliminary investigation of some of the challenges associated with these combined transfer and processing operations, we ran the MFIT in a mode where salt was transferred between both tanks while purification was performed in Tank B. The reactive metal that was employed in the purification consisted of U-Zr-Mo rodlets. The exchange reaction between U metal and a corrosion product in the salt is shown in Equation 8.

$$2U(s) + 3MCl_2(d) \rightarrow 2UCl_3(d) + 3M(s) \qquad \text{Equation 8.}$$

The result should be a stoichiometric increase in fuel salt actinide concentration, and any MC&A approaches must be able to properly quantify the changing composition as the metallic U additive is chlorinated to become UCl_3.

This chemistry control scenario was performed within the MFIT when it nominally contained 2.1 kg of NaCl-KCl-$MgCl_2$-UCl_3 with 3 wt. % UCl_3. Extensive use over the past several years, however, led to the generation of corrosion products in the salt. Figure 31, for example, shows cyclic voltammograms of the MFIT's salt charge at 500 ˚C. Prior to depleted uranium contacting the CVs showed sets of redox peaks corresponding to U/U(III), Cr/Cr(II), Fe(II), and U(III)/U(IV) reactions.

To accomplish chemistry control, a 17.8 g surrogate metal depleted uranium fuel rod was contacted with the chloride salt. The fuel rod, shown in Figure 30, had the composition 87.2% depleted uranium, 11.5% Zr, and 0.7% Mo. It was assumed that the minor alloying elements were not prone to oxidizing readily into the salt. To model a prototypical on-line salt processing facility, the MFIT was operated as a chemical reactor vessel and a holding tank. The depleted uranium rod was added to vessel A which operated as the reactor vessel. Salt was then repeatedly transferred between the reactor vessel and holding vessel (vessel B) to start and stop the reaction between the depleted uranium fuel rod and the chloride salt. To gather statistical data on multimodal sensors, ILEX Automation© software was used to repeatedly cycles through transfers at flow rates between 1 and 10 slpm. The salt was allowed to contact the depleted uranium in the reactor vessel for 5 minutes. The salt was then transferred back into the holding tank where MAVS sensor measurements were recorded.

Figure 30. Depleted uranium-zirconium-molybdenum fuel rod used for salt processing studies in the MFIT

The salt composition was monitored in the salt holding tank in between transfers to the reactor vessel. Figure 31 show the evolution of the composition along with other chemistry-relevant metrics as a function of time the salt was in the reactor vessel. After one hour there is a significant change in the concentration of corrosion products Cr(II) and Fe(II). After 10 hours the peaks corresponding to Cr/Cr(II) and Fe/Fe(II) had disappeared indicating effective purification of corrosion products.

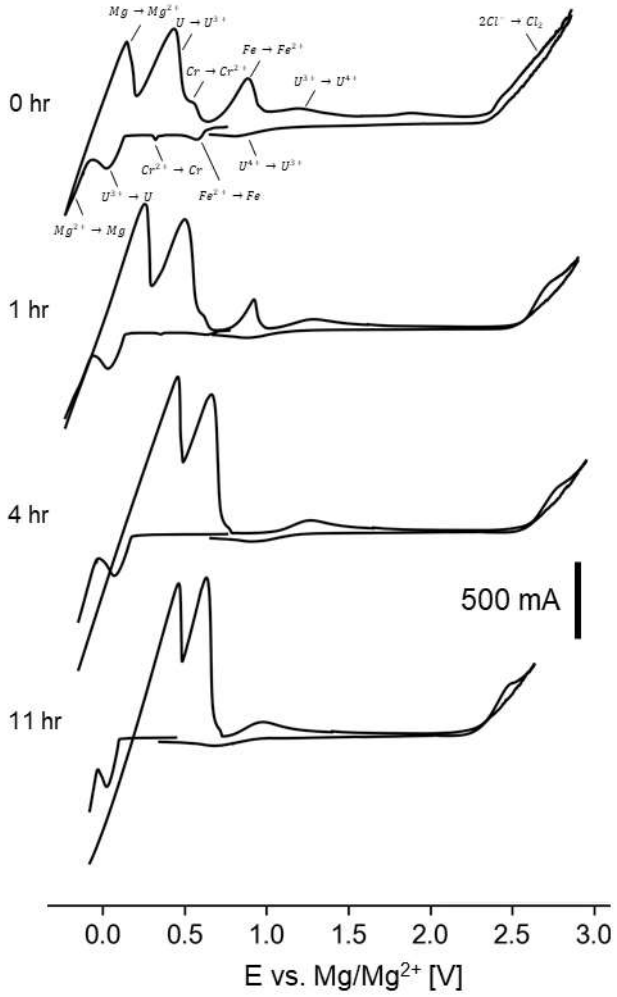

Figure 31. Cyclic voltammetry of NaCl-KCl-$MgCl_2$-UCl_3 (3 wt. % UCl_3) at 500 ˚C after various exposure times to a depleted uranium fuel rod. Scan rate 1000 mV/sec.

The repeatability of the MAVS sensor in Tank B was evaluated in quiescent salt conditions prior to salt purification. Table 4 shows the results of the average of ten complete MAVS measurements. The average salt height was 3.5 ± 0.1 cm, indicating that the tank-to-tank transfers did not result in the loss of any fluid. Although the relative error of the level measurement was high (~3%), the ± 0.1 cm uncertainty is fixed and would result in acceptable error for deeper tanks.

The Cr/Cr(II) and Fe/Fe(II) reactions were identified based on reported reduction potentials [2], and the Cr and Fe concentrations were determined using the diffusion coefficients 7.8 x10^{-6} cm^2 s^{-1} and 9.2 x10^{-6} cm^2 s^{-1}, respectively [2]. The average Cr concentration prior to salt purification was 3.7 ± 0.9 mg/g. The initial

concentration of Fe was 2.1 ± 0.1 mg/g. The concentration of U was calculated by assuming a diffusion coefficient of 1.2 x 10^{-6} cm^2 s^{-1} which yielded an average concentration of 3.2 ± 0.1 wt%.

Table 4. Average of ten multielectrode array voltammetry sensor measurements for in the modular flow instrumentation testbed prior to salt purification.

	Average
Electrode Array Depth [cm]	3.5 ± 0.1 cm
Salt Potential vs. Mg/Mg^{2+}	0.83 ± 0.02 V
$E_{p\ U/U(III)}$ vs. Mg/Mg^{2+}	0.06 ± 0.01 V
$E_{p\ Cr/Cr(II)}$ vs. Mg/Mg^{2+}	0.49 ± 0.04 V
$E_{p\ Fe/Fe(II)}$ vs. Mg/Mg^{2+}	0.56 ± 0.02 V
$j_{U/U(III)}$	-0.239 ± 0.007 A cm^{-2}
$j_{Cr/Cr(II)}$	-0.101 ± 0.008 A cm^{-2}
$j_{Fe/Fe(II)}$	-0.088 ± 0.003 A cm^{-2}
C_U	3.2 ± 0.1 wt%
C_{Cr}	3.7 ± 0.9 mg g^{-1}
C_{Fe}	2.1 ± 0.1 mg g^{-1}

Prior to the addition of depleted uranium to the reactor vessel, the MFIT was operated using ILEX Automation© software to acquire 304 MAVS repeated sensor measurements. During this processing demonstration, 120 salt transfers were made over a range of flow rates to and from the chemical reactor vessel. The MAVS sensor measurements showed excellent repeatability throughout the entire test. Figure 32 depicts trends from the MAVS sensor before and after contacting the salt with the depleted uranium rod in the reactor vessel. During this period over 230 complete transfer cycles to and from the reactor vessel were completed at flow rates between 1 and 10 slpm. The plotted time includes both the residence time in the reactor vessel (5 minutes) and the measurement time in the holding tank approximately (7 minutes). Figure 31 shows the evolution of the MAVS voltammogram 1, 4 and 11 hours after fuel rod addition. Following the addition of the depleted uranium the concentration of corrosion products Cr and Fe dropped to non-detectable levels over the course of 10 hours of processing. The uranium concentration concomitantly increased by 0.5 wt% due to the exchange reaction.

Further analyses are being prepared to fully analyze all the data generated by this demonstration. Salt sampling is also pending to provide complementary composition measurements. Specific attention is being paid toward assessing measurements of the total inventory of uranium located in each tank. Results for this demonstration and others will be included in our planned FY25 reporting after the additional analyses are completed.

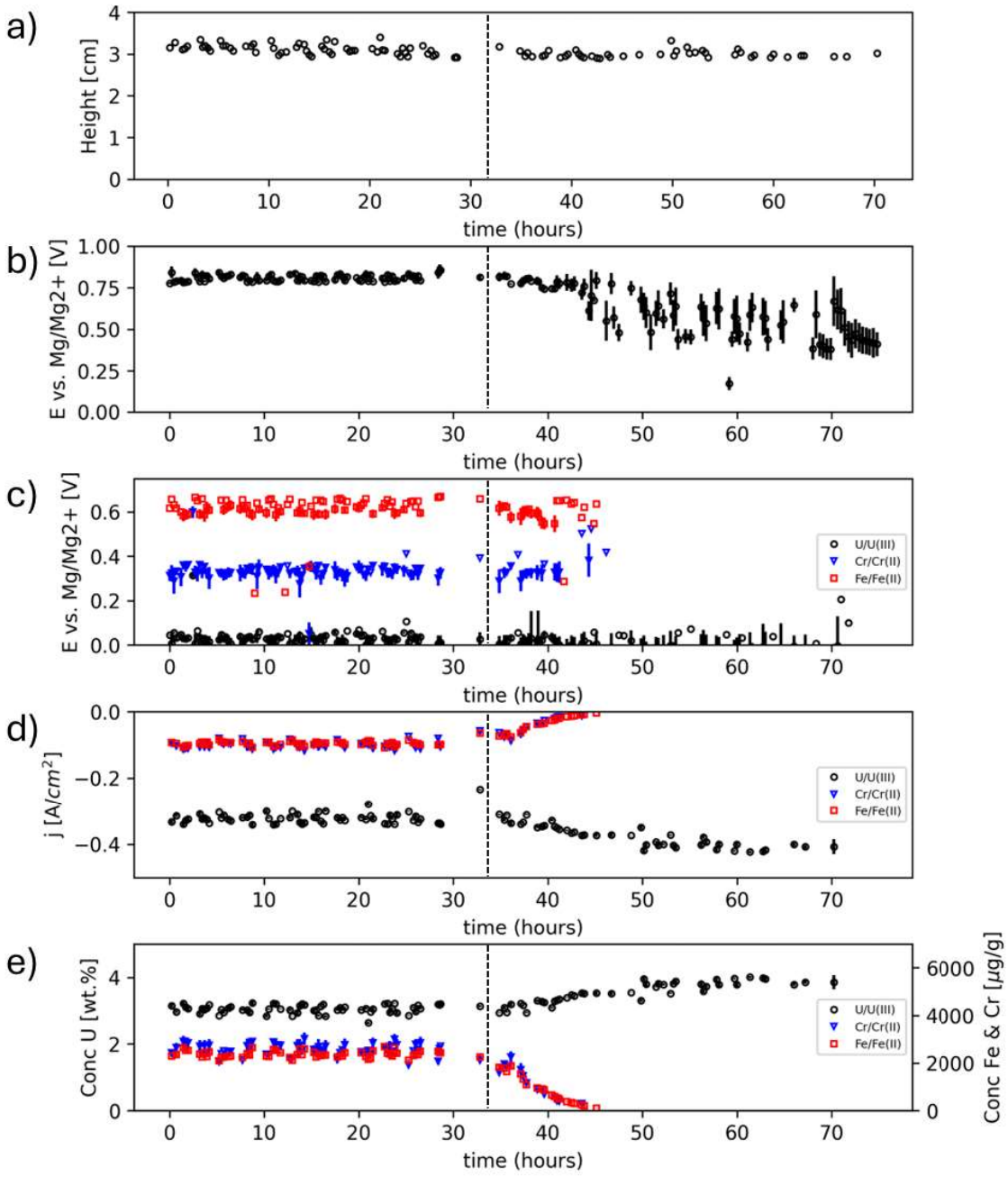

Figure 32. Multielectrode array voltammetry sensor (MAVS) measurements of NaCl-KCl-$MgCl_2$-UCl_3 (3 wt. % UCl_3) during depleted uranium metal contacting including (a) the height of the salt reltive to the MAVS sensor, (b) the average salt redox potential, (c) the reduction peak potential of U/U(III), Cr/Cr(II), and Fe/Fe(II), (d) the cathodic peak current density of of U/U(III), Cr/Cr(II), and Fe/Fe(II) reactions, and (e) the concentration of U(III), Cr(II), and Fe(II).

7. FEES Sensor Deployments

7.1 Flow-Enhanced Electrochemical Sensors at Kairos Power, LLC FLiBe salt test loop

Sensor deployments are included as part of our ARSS activities to provide additional opportunities for sensor shakedown testing. As part of this, Argonne National Laboratory deployed an advanced electrochemical system to Kairos Power's salt test loop in FY24. This activity enabled in-line flow-enhanced electrochemical sensor evaluation in a challenging real-world environment. The Kairos test loop where forced convection operations were performed is shown in Figure 33. This loop contains 15 kg of FLiBe LiF-BeF_2 (66:34 mol %) salt.

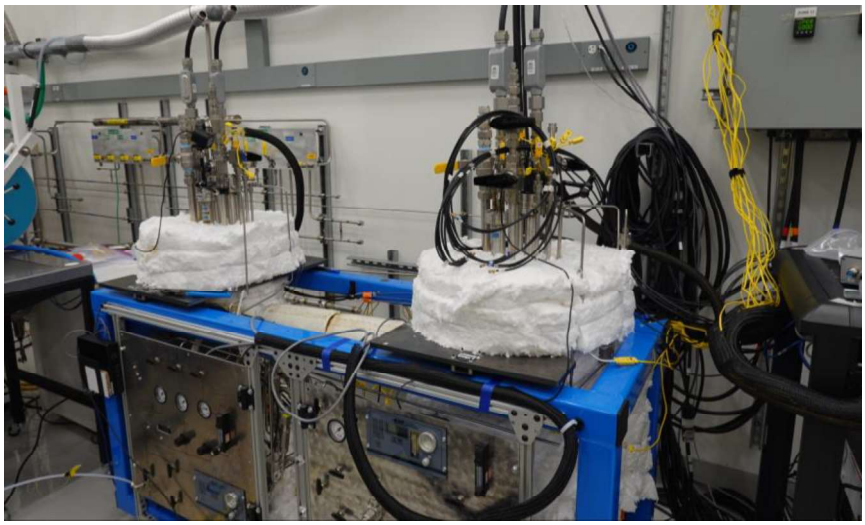

Figure 33. Kairos Power's FLiBe salt test loop

To enable these tests, Argonne successfully engineered and tested a novel electrochemical multiplexer system, shown in Figure 34, which could remotely control up to 12 electrochemical cells in the Kairos test loop. Argonne deployed ILEX Automation© software for electrochemical system automation which facilitated hundreds of semi-autonomous measurements. Argonne additionally provided electrochemical measurement protocols and assisted with data interpretation.

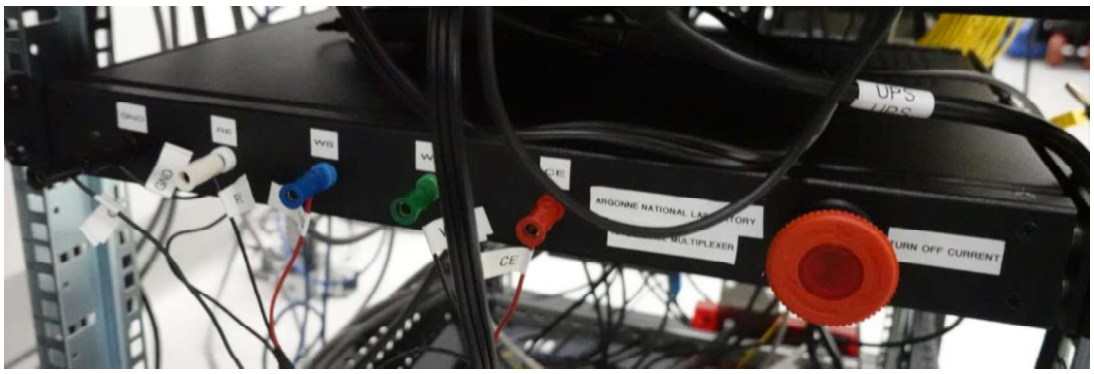

Figure 34. Argonne National Laboratory's custom 12-channel multiplexer for controlling electrochemical sensors in the Kairos test loop.

The flow-enhanced electrochemical sensor placement in the Kairos test loop necessitated sensor design modifications to enable operation in the new environment. The sensors, shown in Figure 35, needed to be adaptable to the new flow path geometry. Precision machining and welding were used to construct sensors that could be inserted into tube section while also maintaining the internal radius. The sensors were carefully sealed to enable them to operate fully submerged and at higher pressures than previously encountered. Figure 36 shows the temperature of the two flow-enhanced electrochemical sensors over the duration of loop activities. The sensors endured over 900 hours of loop operations without noticeable damage or leaks.

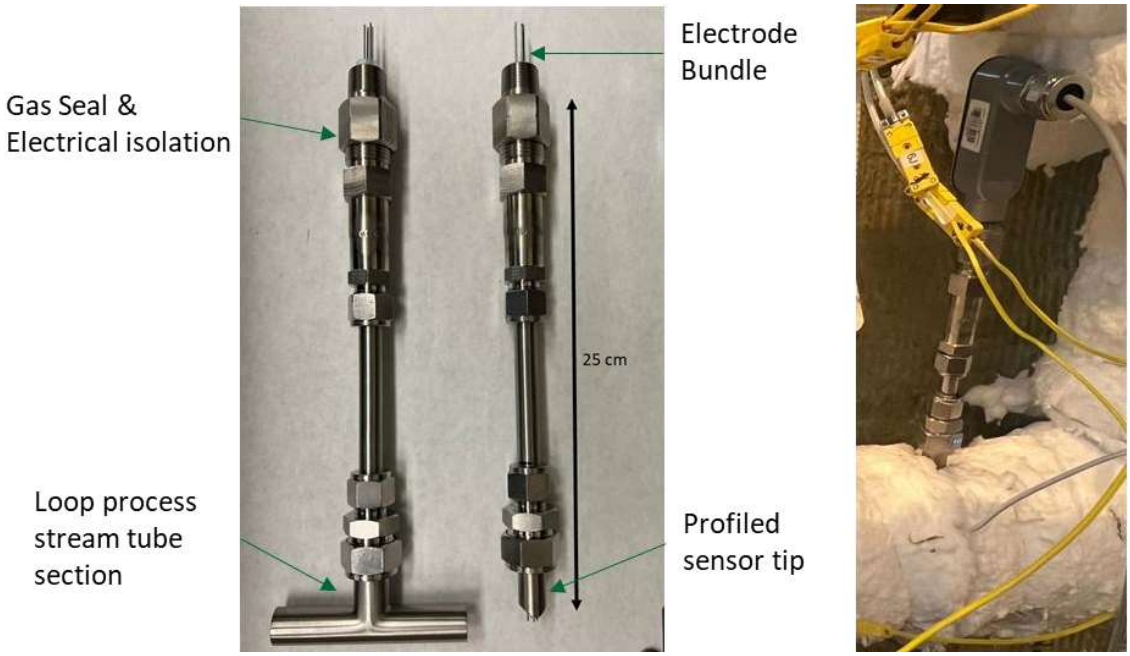

Figure 35. In-line flow-enhanced electrochemical sensors installed in Kairos Power's test loop.

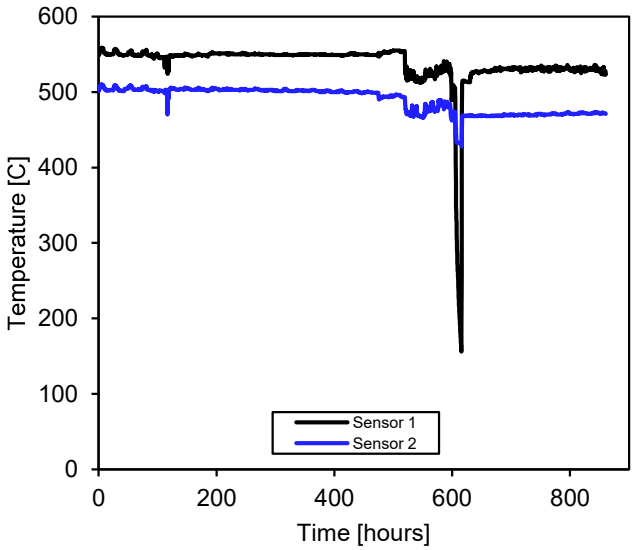

Figure 36. Temperatures near the two in-line electrochemical sensors.

Crucial data regarding the composition of the FLiBe salt, fluid flow, and the structural health of the salt test loop were obtained from the flow-enhanced electrochemical sensors. Figure 14 shows an example of a typical voltammogram obtained from the sensors during loop operations. In order to protect Kairos Power's intellectual property, the potential axis has purposefully been removed. Salt composition and fluid flow measurements were conducted periodically during steady state loop operation with both natural convection and forced flow circulation. The chemistry of the FLiBe salt was very stable during operations. There were minimal changes in salt redox potential or dissolved metal ion concentrations. The electrochemical monitoring ultimately provided key insights into long-term operations of Kairos' molten salt equipment.

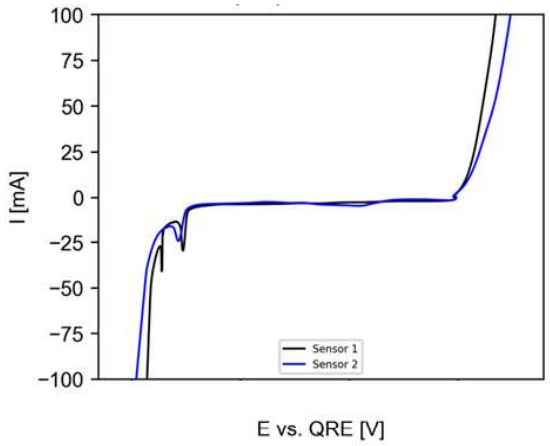

Figure 37. In-line electrochemical sensor voltammetry measurements of circulating FLiBe salt in the Kairos test loop.

7.2 Sensor Deployment to TerraPower LLC

In FY24, Argonne National Laboratory and TerraPower, LLC. established a nondisclosure agreement for the purposes of collaboration on deployment of Argonne's electrochemical sensors in engineering-scale molten chloride salt experiments. The objective of this agreement was to provide additional opportunities for testing Argonne's sensors in real-world systems and to increase the technology readiness of the associated instrumentation.

Toward that end, Argonne has constructed two electrochemical sensors that have been designed to be mated to a molten salt loop at TerraPower's molten salt testing laboratory. Figure 38 shows the sensors and Argonne's custom four-channel multiplexer that is used to support signaling across the electrode arrays. Argonne will also deploy its ILEX Automation© software to facilitate semiautonomous salt measurements and help train TerraPower staff on sensor operations. Fabrication of the equipment was completed in late FY24, and sensor operations are expected to begin in FY25 Q1.

Figure 38. A pair of multielectrode array voltammetry sensors (MAVS) for deployment at TerraPower, LLC. Argonne National Laboratory's custom 4-channel Multiplexer for controlling two multielectrode array voltammetry sensors (MAVS).

8. CONCLUSIONS

In FY24 significant progress toward the development of FEES for nuclear materials accountancy was made including the development of techniques to measure concentrations of high concentration actinide salts, the integration of new multimodal sensors in the MFIT, and the deployment of FEES in challenging real-world environments at partner institutions. By implementing multimodal sensors including a stationary salt chemistry sensor and a flow rate sensor, FEES concentration measurements were improved to a mean absolute standard error of 2.5% compared to 3.1% in FY23.

Using improved automation approaches, these techniques were demonstrated at a high accuracy and rate of acquisition during a salt purification process with safeguards relevance. The sensors yielded practical knowledge about the evolution of the salt composition during purification as well insights into possible safeguards challenges. Key findings included monitoring that indicated the concentration of UCl_3 increased stoichiometrically with the amount of corrosion products that were removed. If such a method for salt redox control were utilized in an operational MSR, close coupling between corrosion control operations and materials control and accountancy activities would need to be implemented to ensure sufficient accuracy to meet the regulatory requirements.

Experiments in a high-concentration actinide-bearing chloride salts were also carried out to validate electroanalytical techniques. A LiCl-KCl-UCl_3 salt with concentrations as high as 72 wt% U was used for this research. In the quiescent salt conditions, it was observed that supporting digital simulations were able to address the nonidealities present at the extreme concentrations and achieve accurate values. Relative systematic and random errors for measurements at these concentrations were fair (4.7% and 1.3%, respectively), but future work will aim to refine the current multiplier model with additional data.

To support high-concentration flow testing in the MFIT, a small-scale batch of NaCl-UCl_3 was produced by chlorination of U metal using $ZnCl_2$. The process led to a greater than 80 % reaction completion based on the mass change of the depleted uranium ingot. Analysis of the product is still ongoing. This preliminary salt production process showed promise for producing the large-scale batch of high concentration UCl_3 salt. Preparations have been made at Argonne to use depleted uranium powders currently in inventory for production of the 2.0 liters of salt needed for MFIT operations.

Finally, Argonne successfully deployed two in-line flow-enhanced electrochemical sensors at one partner institution and has constructed sensors for deployment at another. The deployed FEES sensors operated in flowing molten salt for over 900 hours without any faults. Two new electrochemical sensors are scheduled to be shipped to the second partner institution in early FY25.

REFERENCES

[1] N. C. Hoyt, M. A. Williamson, and J. L. Willit, "Multielectrode sensor for concentration and depth measurements in molten salt," Argonne National Laboratory (ANL), Argonne, IL (United States), 10,955,375, Mar. 2021. Accessed: Jan. 28, 2024. [Online]. Available: https://www.osti.gov/biblio/1805658

[2] J. Guo, N. Hoyt, and M. Williamson, "Multielectrode array sensors to enable long-duration corrosion monitoring and control of concentrating solar power systems," *J. Electroanal. Chem.*, vol. 884, p. 115064, Mar. 2021, doi: 10.1016/j.jelechem.2021.115064.

[3] N. C. Hoyt, J. L. Willit, and M. A. Williamson, "Communication—Quantitative Voltammetric Analysis of High Concentration Actinides in Molten Salts," *J. Electrochem. Soc.*, vol. 164, no. 2, p. H134, Jan. 2017, doi: 10.1149/2.1481702jes.

[4] J. Lubbers, "A Raman Spectroscopy-Based In Situ Composition Monitoring System for Molten Salt Reactors," Sporian Microsystems, Inc., Lafayette, CO (United States), 600-000-0622–00, Jan. 2019. Accessed: Sep. 29, 2024. [Online]. Available: https://www.osti.gov/biblio/1491583

[5] A. M. Lines, S. D. Branch, H. M. Felmy, J. M. Wilson, G. J. Lumetta, and S. A. Bryan, "On-line monitoring combined with spectroelectrochemistry for the characterization of uranium and fission products within molten salt environments," Pacific Northwest National Lab. (PNNL), Richland, WA (United States), PNNL-SA-144352, Jan. 2020. Accessed: Sep. 29, 2024. [Online]. Available: https://www.osti.gov/biblio/1606192

[6] J. Sanders *et al.*, "Experimental Validation Of NDA Capabilities For MSR Safeguards: First Results |," in *Proceedings of the INMM & ESARDA Joint Virtual Annual Meeting*, Aug. 2021. Accessed: Sep. 29, 2024. [Online]. Available: https://resources.inmm.org/annual-meeting-proceedings/experimental-validation-nda-capabilities-msr-safeguards-first-results

[7] E. Lukosi, "Microfluidic Alpha Spectrometry of UOX PWR UNF in a Molten Salt," *Nucl. Sci. Eng.*, vol. 188, no. 3, pp. 294–302, Dec. 2017, doi: 10.1080/00295639.2017.1367248.

[8] S. Maji, S. Kumar, and K. Sundararajan, "Exploring LIBS for simultaneous estimation of Sr, Ba and La in LiCl-KCl salt," *Optik*, vol. 207, p. 163801, Apr. 2020, doi: 10.1016/j.ijleo.2019.163801.

[9] C. Moore, W. Doniger, and N. Hoyt, "Assessment of Flow-Enhanced Electrochemical Sensor Testing and Deployments for MSRs," ANL/CFCT-23/38, Sep. 2023.

[10] K. K. Hogue, N. Luciano, M. Krupcale, R. Elzohery, and L. G. Evans, "Planning for Material Control and Accountancy at Liquid Fueled Molten Salt Reactors," Oak Ridge National Laboratory (ORNL), Oak Ridge, TN (United States), ORNL/SPR-2023/3181, Jan. 2024. doi: 10.2172/2283859.

[11] J. C. Gehin, D. E. Holcomb, G. F. Flanagan, B. W. Patton, R. L. Howard, and T. J. Harrison, "Fast Spectrum Molten Salt Reactor Options," Oak Ridge National Lab. (ORNL), Oak Ridge, TN (United States), ORNL/TM-2011/105, Jul. 2011. doi: 10.2172/1018987.

[12] W. E. Miller and Z. Tomczuk, "Method for making a uranium chloride salt product," Argonne National Laboratory (ANL), Argonne, IL (United States), 6,800,262, Oct. 2004. Accessed: Sep. 22, 2024. [Online]. Available: https://www.osti.gov/doepatents/biblio/935569

[13] A. M. Bond, S. W. Feldberg, H. B. Greenhill, and P. J. Mahon, "Instrumental, theoretical, and experimental aspects of determining thermodynamic and kinetic parameters from steady-state and non-steady-state cyclic voltammetry at microelectrodes in high-resistance solvents: Application to the fac/mer-[Cr(CO){sub 3}({eta}{sup 3}-Ph{sub 2}PCH{sub 2}CH{sub 2}P(Ph)CH{sub 2}CH{sub 2}PPh{sub 2})]{sup +/0} square reaction sheme in dichloromethane," *Anal. Chem. Wash.*, vol. 64, no. 9, May 1992, doi: 10.1021/ac00033a010.

[14] F. Scholz, *Electroanalytical Methods: Guide to Experiments and Applications*, 1st ed. Springer Berlin Heidelberg, 2002.

[15] N. C. Hoyt, J. L. Willit, and M. A. Williamson, "Communication—Quantitative Voltammetric Analysis of High Concentration Actinides in Molten Salts," *J. Electrochem. Soc.*, vol. 164, no. 2, p. H134, Jan. 2017, doi: 10.1149/2.1481702jes.

[16] N. Shaheen, J. Guo, and N. C. Hoyt, "Development and Assessment of Deployed Sensors and Technologies Supporting Molten Salt Loop Operations," ANL/CFCT-24/28, Sep. 2024.
[17] D. Inman, G. J. Hills, L. Young, and J. O. Bockris, "Electrode reactions in molten salts: the uranium + uranium trichloride system," *Trans. Faraday Soc.*, vol. 55, no. 0, pp. 1904–1914, Jan. 1959, doi: 10.1039/TF9595501904.
[18] T. A. Johnson, D. V. Laug, S. X. Li, and T. Sofu, "Experimental observations on electrorefining spent nuclear fuel in molten LiCl-KCl/liquid cadmium system.," 3rd International Symposium on New Materials, Montreal, Quebec (CA), 07/04/1999--07/08/1999. Accessed: Sep. 19, 2024. [Online]. Available: https://digital.library.unt.edu/ark:/67531/metadc622283/
[19] B. R. Westphal and R. D. Mariani, "Method for the production of uranium chloride salt," Idaho National Laboratory (INL), Idaho Falls, ID (United States), 8,475,756, Jul. 2013. Accessed: Jun. 21, 2024. [Online]. Available: https://www.osti.gov/doepatents/biblio/1087860
[20] H. Lambert, T. Kerry, and C. A. Sharrad, "Preparation of uranium(III) in a molten chloride salt: a redox mechanistic study," *J. Radioanal. Nucl. Chem.*, vol. 317, no. 2, pp. 925–932, Aug. 2018, doi: 10.1007/s10967-018-5953-7.
[21] P. Masset *et al.*, "Electrochemistry of Uranium in the Molten LiCl-KCl Eutectic," *J. Electrochem. Soc.*, Sep. 2005, Accessed: Sep. 19, 2024. [Online]. Available: https://publications.jrc.ec.europa.eu/repository/handle/JRC30471
[22] C. H. Lee, T.-J. Kim, D. Yoon, J. Jang, G.-Y. Kim, and S.-J. Lee, "Efficient preparation of UCl3 by ZnCl2 mediated chlorination," *J. Radioanal. Nucl. Chem.*, vol. 322, no. 2, pp. 331–336, Nov. 2019, doi: 10.1007/s10967-019-06782-5.
[23] M. A. Rose, L. D. Gardner, T. T. Lichtenstein, S. A. Thomas, and E. Wu, "Property Measurements of NaCl-UCl3 and NaCl-KCl-UCl3 Molten Salts (Rev.1)," Argonne National Laboratory (ANL), Argonne, IL (United States), ANL/CFCT-22/45-Rev.1, May 2023. doi: 10.2172/1985295.
[24] H. Zhang, M. L. Newton, D. E. Hamilton, and M. F. Simpson, "High temperature UCl3 synthesis in molten salt mixtures via reaction of U metal with iron chlorides," *J. Radioanal. Nucl. Chem.*, vol. 331, no. 1, pp. 383–390, Jan. 2022, doi: 10.1007/s10967-021-08060-9.
[25] Y. Sakamura, T. Inoue, T. Iwai, and H. Moriyama, "Chlorination of UO2, PuO2 and rare earth oxides using ZrCl4 in LiCl–KCl eutectic melt," *J. Nucl. Mater.*, vol. 340, no. 1, pp. 39–51, Apr. 2005, doi: 10.1016/j.jnucmat.2004.11.002.
[26] P. Chiotti, "The U−Zn (Uranium-Zinc) system," *Bull. Alloy Phase Diagr.*, vol. 1, no. 2, pp. 110–113, Sep. 1980, doi: 10.1007/BF02881208.
[27] J. Guo, N. Hoyt, and M. Williamson, "Multielectrode Array Sensors to Enable Long-Duration Corrosion Monitoring and Control of Concentrating Solar Power Systems," *J. Electroanal. Chem.*, p. 115064, Feb. 2021, doi: 10.1016/j.jelechem.2021.115064.
[28] C. F. Baes, "The chemistry and thermodynamics of molten salt reactor fuels," *J. Nucl. Mater.*, vol. 51, no. 1, pp. 149–162, May 1974, doi: 10.1016/0022-3115(74)90124-X.
[29] A. Worrall *et al.*, "Molten Salt Reactors and Associated Safeguards Challenges and Opportunities," Oak Ridge National Laboratory (ORNL), Oak Ridge, TN (United States), Nov. 2018. Accessed: Sep. 29, 2024. [Online]. Available: https://www.osti.gov/biblio/1630525